



(Unterschrift Betreuer/in)

Diplomarbeit

Suszeptibilitätsgewichtete Bildgebung des Knies

ausgeführt am

Atominstitut

der Technischen Universität Wien

unter der Anleitung von

Univ. Prof. DI Dr. techn. Gerald Badurek

In Zusammenarbeit mit

Ass. Prof. Dr. Simon Robinson

**Exzellenzzentrum für Hochfeld-Magnetresonanz,
Universitätsklinik für Radiologie und Nuklearmedizin**

Medizinische Universität Wien

durch

Paul Schennach

Meidlinger Hauptstraße 84/2/6

Wien, 16. Dezember 2015

(Unterschrift Verfasser)



TECHNISCHE
UNIVERSITÄT
WIEN
Vienna University of Technology

(Signature of Advisor)

Master's Thesis

Susceptibility Weighted Imaging of the Knee

performed at the

Atominstitut

of the Technische Universität Wien

under the guidance of

Univ. Prof. DI Dr. techn. Gerald Badurek

in cooperation with

Ass. Prof. Dr. Simon Robinson

MR Centre of Excellence,

Department of Biomedical Imaging and Image-guided Therapy

Medical University of Vienna

by

Paul Schennach

Meidlinger Hauptstraße 84/2/6

Vienna, December 16th, 2015

(Signature of Author)

Erklärung zur Verfassung der Arbeit

Paul Schennach
Meidlinger Hauptstraße 84/2/6, 1120 Wien

Hiermit erkläre ich, dass ich diese Arbeit selbstständig verfasst habe, dass ich die verwendeten Quellen und Hilfsmittel vollständig angegeben habe und dass ich die Stellen der Arbeit – einschließlich Tabellen und Abbildungen –, die anderen Werken oder dem Internet im Wortlaut oder dem Sinn nach entnommen sind, auf jeden Fall unter Angabe der Quelle als Entlehnung kenntlich gemacht habe.

(Ort, Datum)

(Unterschrift Verfasser)

Acknowledgment

First and foremost I want to thank Ass.Prof. Dr. Simon Robinson for guiding me through this diploma project. I also want to acknowledge the support of his PhD students Dipl.Ing. Barbara Dymerska and Pedro Cardoso MSc. Also I want to thank all the young subjects participating in the measurements and the radiographers Claudia Kronnerwetter and Manuela Karner for providing their expertise. I am grateful to have had Univ.Prof. DI Dr.techn. Gerald Badurek and Ass.Prof. DI Dr. Karin Poljanc as my supervisors at the part of the Technische Universität Wien.

Special thanks go to my parents Mag. Klaus Schennach and Dipl.Päd. Ingrid Schennach who supported me throughout my studies, without whom this work would not have been possible.

Abstract

Susceptibility weighted imaging (SWI) [1] is a magnetic resonance imaging (MRI) method which utilizes the phase part of the MR signal to increase contrast for tissues of different susceptibility. However, phase is not an accurate map of the underlying susceptibility, due to non-local effects. Therefore dedicated algorithms have been established which recover susceptibility from phase - a process known as quantitative susceptibility mapping (QSM). Employing susceptibility instead of phase for the use in SWI avoids artefacts and improves visualization of different tissues. To date, SWI and QSM have been predominantly used for neuroimaging, but there is also high potential for imaging cartilage in joints. Visualizing veins and the multizonal structure within the infantile knee cartilage could help to understand and diagnose the development of ossification disorders like osteochondritis dissecans (OD). This project aimed to generate the first in vivo SWI of growing human knee cartilage at ultra-high field (UHF). For data acquisition a gradient echo (GE) sequence was optimized using a phased array of multiple coils. The quality of SWI relies on the correct reconstruction of individual phase images from multiple coils. Therefore numerous approaches to combine data from a phased array have been implemented and assessed, in order to obtain the optimum reconstruction pipeline for high-quality SWI of the human knee cartilage. Venous vasculature and zones within infantile knee cartilage was visualized in vivo using SWI and QSM, which constitutes a promising finding for future MRI-studies on ossification disorders.

Kurzfassung

Die suszeptibilitätsgewichtete Bildgebung (SWI) [1] ist eine Magnetresonanz (MR)-Bildgebungsmethode, welche die Phase des MR-Signals verwendet, um den Kontrast zwischen Geweben unterschiedlicher Suszeptibilität zu verstärken. Aufgrund von nicht-lokalen Effekten stellt die Phase allerdings keine genaue Abbildung der zugrunde liegenden Suszeptibilität dar. Aus diesem Grund wurden aufwendige Algorithmen entwickelt, welche die Suszeptibilitätsverteilung aus der Phaseninformation extrahieren – ein Prozess der quantitative Suszeptibilitätsabbildung (QSM) genannt wird. Durch die Verwendung der Suszeptibilität, anstelle der Phase für SWI, werden Artefakte vermieden sowie die Visualisierung unterschiedlicher Gewebe verbessert. Bisher wurden SWI und QSM fast ausschließlich für die Neurobildgebung verwendet, wobei beide Verfahren auch großes Potential für die Bildgebung von Gelenksknorpel bergen. Die Visualisierung des venösen Gefäßsystems im kindlichen Knieknorpel könnte zum Verständnis der Entwicklung von Ossifikationsstörungen, wie beispielsweise der Osteochondritis Dissecans (OD), beitragen und eine frühere Erkennung dieser ermöglichen. Die vorliegende Arbeit hatte das Ziel, die erste in vivo SWI-Bildgebung am wachsenden menschlichen Knieknorpel bei ultra-hoher Feldstärke zu entwickeln. Hierfür wurde einerseits die Datenaufnahme mithilfe einer Gradientenecho (GE)-Sequenz für eine Mehrkanalspule optimiert, und andererseits mehrere Verfahren zur Kombination der Mehrkanal-Einzelbilder implementiert und evaluiert, um die optimale Datenverarbeitung für SWI am Kniegelenk zu bestimmen. Venen und Wachstumszonen im kindlichen Knieknorpel konnten mithilfe von SWI und QSM visualisiert werden, was ein vielversprechendes Resultat für zukünftige MR-Studien zu Ossifikationsstörungen darstellt.

List of Acronyms

AR	Aspect Ratio (voxel geometry)
CNR	Contrast to Noise Ratio
COMPOSER	<u>C</u> ombining <u>P</u> hased array data using <u>O</u> ffsets from a <u>S</u> hort <u>E</u> cho-time <u>R</u> eference scan
FOV	Field Of View
GE	Gradient Echo sequence
GRAPPA	<u>G</u> eneral <u>A</u> utocalibrating <u>P</u> artially <u>P</u> arallel <u>A</u> cquisitions
MCPC-C	Multi-channel phase combination using constant phase offsets
mIP	minimum Intensity Projection
MRI	Magnetic Resonance Imaging
PHUN	<u>P</u> hase <u>U</u> nwrapping (algorithm)
PRELUDE	<u>P</u> hase <u>R</u> egion <u>E</u> xpanding <u>L</u> abeller for <u>U</u> nwrapping <u>D</u> iscrete <u>E</u> stimates (algorithm)
QSM	Quantitative Susceptibility Mapping
RF	Radio Frequency
RPO	Reference Phase Offset
SAR	Specific Absorption Ratio (RF power deposition)
SNR	Signal to Noise Ratio

SWI	Susceptibility Weighted Imaging
TE	Echo Time
TR	Repetition Time
tSWI	true Susceptibility Weighted Imaging
TV	Total Variation
UHF	Ultra High Field (7T or higher)
VRC	Virtual Reference Coil

Contents

1	Motivation	1
2	Aims and Hypothesis	4
3	Introduction	4
3.1	Physics of Magnetic Resonance	4
3.1.1	Magnetic Moment - Spin	4
3.1.2	RF Pulse Excitation	6
3.1.3	Relaxation Phenomena	7
3.2	Magnetic Resonance Imaging	9
3.2.1	Encoding	9
3.2.2	Image Formation	11
3.2.3	Gradient Echo Sequence	12
3.3	Imaging with Phased Array RF Coils	13
3.3.1	Phase in MRI	17
4	Theory	20
4.1	Reconstructing Multiple Coil Data	20
4.1.1	Homodyne Filter	21
4.1.2	Multiple Coil Phase Combination with Constant Offsets (MCPC- C)	22
4.1.3	Virtual Reference Coil Approach (VRC)	23
4.1.4	Using Phase Offsets From a Short Reference Scan (COM- POSER)	26
4.1.5	The Adaptive Combine Approach	27

4.2	Phase Unwrapping	30
4.2.1	Spatial Unwrapping	30
4.2.2	PRELUDE Unwrapping	30
4.2.3	Fourier-Based Unwrapping	31
4.3	Susceptibility Weighted Imaging	33
4.4	Quantitative Susceptibility Mapping	35
4.5	True SWI	36
5	Materials and Methods	37
5.1	MR Measurements	38
5.1.1	T2* - Mapping	38
5.1.2	SWI - Sequence	39
5.1.3	Variable Echo Time Sequence	40
5.2	Reconstruction Pipeline	40
5.2.1	Strategy 1: Single Coil Unwrapping and Weighted Mean Com- bination	42
5.2.2	Strategy 2: Phase Matching by Removing Phase Offsets	42
5.3	SWI - Processing	43
5.4	Analysis	43
5.4.1	Phase Matching	43
5.4.2	SWI Results	44
5.5	QSM - Algorithm	45
5.6	True SWI - Processing	45

6	Results	46
6.1	T2*-Maps of Knee Cartilage	46
6.2	Combination of Multiple Coil Data	47
6.2.1	Single Coil Unwrapping and Weighted Mean Combination (Strategies 1a and 1b)	47
6.2.2	Phase Matching by Removing Phase Offsets (Strategies 2a, 2b and 2c)	49
6.3	Susceptibility Weighted Images	51
7	Discussion	59
8	Conclusion	61
	References	62

1 Motivation

During growth, the knee joint is subject to ongoing ossification of cartilage, which denotes the transition of cartilaginous tissue to bone near the surface of the bone. Ossification takes place in the epiphyseal (primary) physis and around the chondroepiphysis (secondary physis), which forms the distal end of long bones (Fig.1). The process of ossification is enabled by vascularized cartilage canals near the ossification centres (Fig.3). The arteries perfusing the cartilage provide osteoblasts and osteoclasts which erode cartilaginous tissue and build bone (Fig.2). In the course of aging, bone tissue grows while cartilage becomes thinner and less vascularized.

Disorders in the ossification process may result in diseases such as osteochondroses and osteochondritis dissecans (OD). Such disorders are assumed to result from insufficiently perfused cartilage canals, as has been reported in animal studies [2]. The different stages in the development of osteochondroses are explained by a model introduced in Ref.[3] and shown in Fig.4. At an early age, articular cartilage is well vascularized (Fig.4A). During growth the ossification front advances (Fig.4B) and vessels from the ossification centre connect with vessels in the cartilage. Therefore, blood supply of the cartilage is more and more adopted by vessels originating in the ossification front. An interruption of such a vessel reduces the blood supply of a certain area (Fig.4C and 4D) and may cause ischemic necrosis of the cartilage. If the affected area is small (Fig.4E), this is likely to be vascularized again by the surrounding ossification front and the bone growth continues without damage. When the affected area is bigger (Fig.4F), re-vascularization and ossification is not possible, and the necrotic cartilage forms a cone within the bone. In the process of aging, such a lesion may become enclosed entirely by bone tissue (Fig.4H) and replaced by fibrous tissue over time. However, in some cases the underlying articular cartilage will rupture (Fig.4I), forming an osteochondritis dissecans lesion. The etiology and pathophysiology of ossification disorders in humans is still not fully clarified. In vivo imaging of vessels in growing cartilage could give more insight into this, and

may help to diagnose and classify the ossification disorder at hand at an early stage, which would support the difficult decision for appropriate therapy. Therefore, MR imaging of juvenile knee cartilage using susceptibility weighted imaging (SWI) to visualize veins is a promising technique, especially because no contrast agents are involved.

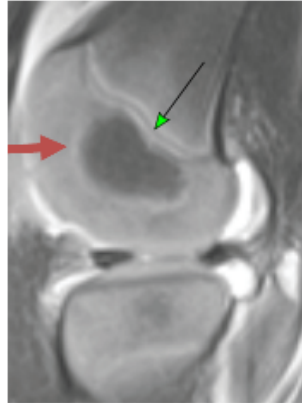


Figure 1: MR image of the knee of a two year old child. The green arrow points to the primary physis, which separates the metaphysis from the chondroepiphysis. The dark area in the chondroepiphysis is the ossification centre, which is surrounded by a line of high signal intensity which is the secondary physis (red arrow) (courtesy of Univ.Prof. Dr. Klaus Bohndorf, Meduni Wien).

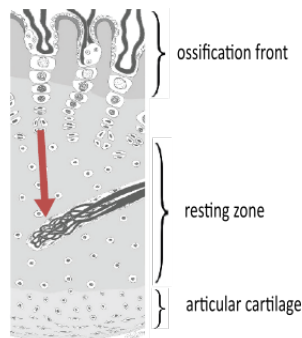


Figure 2: Cross section of an articular cartilage complex. The red arrow points to a cartilage canal comprising a blood vessel (reproduced from Ref.[3]).

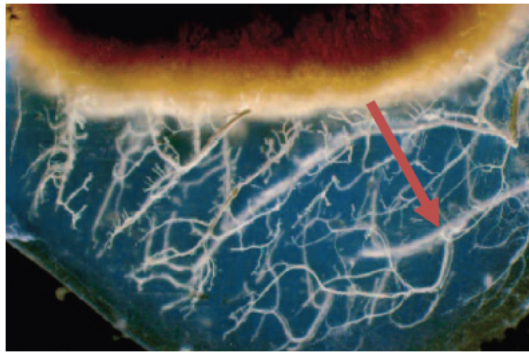


Figure 3: A transillumination image of articular cartilage from a 7-week-old piglet, showing that cartilage tissue (bluish) is well vascularized (reproduced from Ref.[3]).

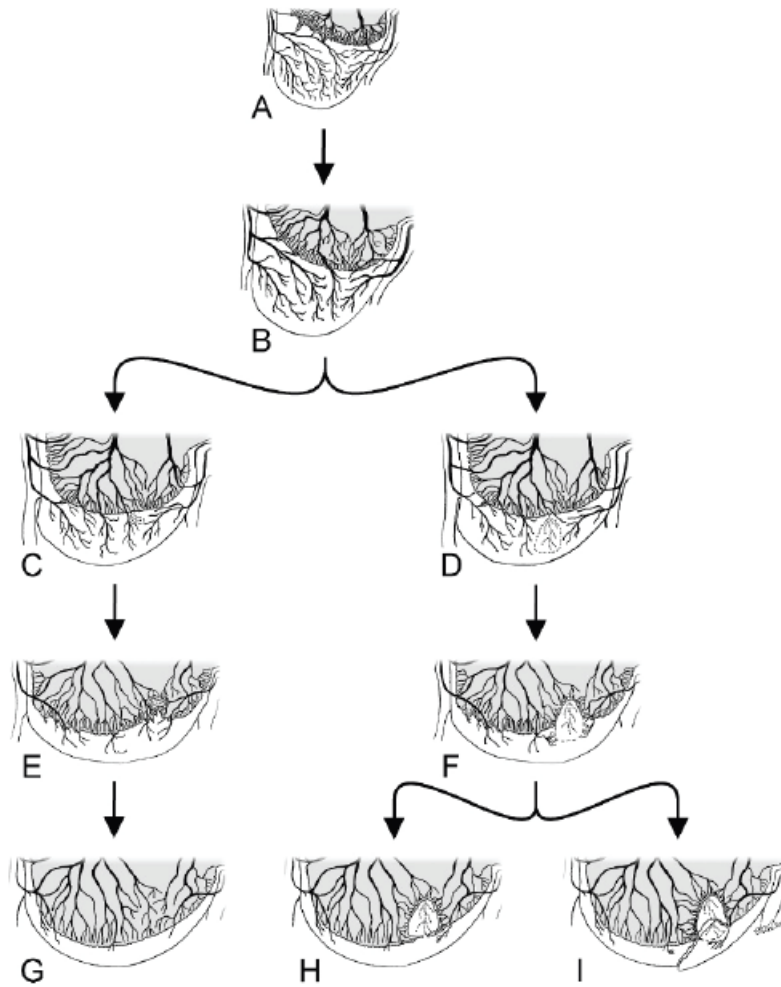


Figure 4: Stages in the development of ossification disorders in articular cartilage (reproduced from Ref.[3]).

2 Aims and Hypothesis

This project aimed to establish SWI in the complicated magnetic environment of the knee at ultra high field for the first time, in order to visualize veins in the growing knee cartilage of young healthy volunteers. A gradient echo (GE) sequence was optimised for data acquisition, and a variety of post-processing approaches were implemented and assessed for quality. SWI of the knee could open up the possibility to observe and quantify changes in the vessel density of patients suffering from ossification disorders, which would allow early detection of vessel disturbances and their progression. Once this technique is made useful for clinical practice, this would certainly benefit future health care.

3 Introduction

3.1 Physics of Magnetic Resonance

Magnetic Resonance Imaging (MRI), is a noninvasive imaging technique widely used in modern medicine. MRI makes use of the magnetic dipole moment of nucleons, which arises from their intrinsic angular momentum – the so called spin. By manipulation of the orientation of the spins with the help of magnetic and electromagnetic fields, images from the inside of patients are produced. Contrast among different tissues originates from specific physical properties, such as the proton density and the relaxation time constants T_1 , T_2 and T_2^* .

3.1.1 Magnetic Moment - Spin

The magnetic moment of a nucleon is associated with its spin. This relation is described by:

$$\vec{\mu} = \gamma \vec{I} = g_I \mu_K \frac{\vec{I}}{\hbar} \quad (3.1)$$

where $\vec{\mu}$ is the magnetic moment, \vec{I} is the spin, and γ is the gyromagnetic ratio, which describes the proportionality of a nucleons' mechanical and electromagnetic properties, the nuclear g - factor g_I and the nuclear magneton μ_K .

It is well known from quantum physics that the magnitude of the spin is quantized. Furthermore, in a magnetic field \vec{B}_z with its field lines along the z-axis, the orientation of the spin to \vec{B}_z is quantized too - i.e. the spin can only have discrete z-components I_z , which are described by the quantum number m_I (see Fig.5) :

$$|\vec{I}| = \sqrt{I(I+1)}\hbar \quad I = 0, \frac{1}{2}, 1, \frac{3}{2}, \dots \quad (3.2)$$

$$I_z = m_I \hbar \quad m_I = -I, -I+1, \dots, I-1, I \quad (3.3)$$

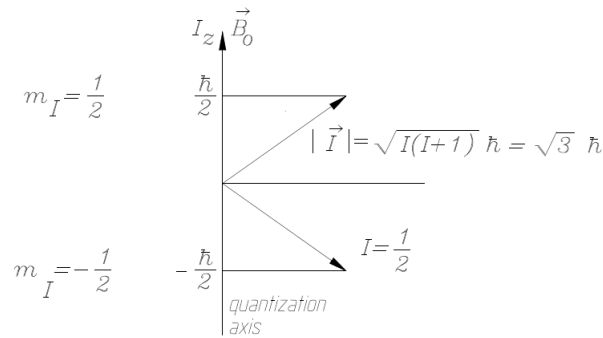


Figure 5: Spin quantization in an external field (reproduced from lectures notes “Biological and Medical Applications of Nuclear Physics 2” by Univ.Prof. DI Dr.techn. Gerald Badurek, 2013).

The quantization of the spin holds also for the magnetic moment, as can be seen from Eq.(3.1). The interaction of $\vec{\mu}$ with a magnetic field leads to a precession of the spin around the field lines and constitutes a potential energy W , which is determined by the orientation of $\vec{\mu}$ to the magnetic field:

$$W = -\vec{\mu} \vec{B}_0 \quad (3.4)$$

The quantized orientations of $\vec{\mu}$ lead to discrete energy eigenvalues E_{m_I} for the nucleus residing in a magnetic field:

$$E_{m_I} = -\gamma \hbar B_0 m_I \quad (3.5)$$

The difference between two energy states ΔE increases with field strength (Zeeman-effect) and is given by:

$$\Delta E = \gamma \hbar B_0 = \hbar \omega_0 \quad (3.6)$$

where ω_0 is the precession frequency of the spin and is called Larmor frequency. Transitions between Zeeman-levels are possible by absorption or emission of photons, in which case the photon energy must equal ΔE . Therefore, the spin orientation of a nucleon inside a magnetic field can be flipped by interaction with an electromagnetic wave having the Larmor frequency, which is called nuclear resonance - the basis for MRI.

3.1.2 RF Pulse Excitation

For imaging it is necessary to flip the magnetization towards the transverse plane (the xy-plane), which is the plane perpendicular to the spins aligned with the main magnetic field B_0 in z-direction, in order to measure the relaxation of the magnetization back into the equilibrium state. This is done by irradiating the sample with a transverse radio frequency field (RF). The RF-field tilts the magnetization towards

the xy-plane and increases the y-component M_y while decreasing the z-component M_z . The amount of tilt is determined by the amplitude and the duration of the RF-field, which is denoted as B_1 in the following, and is given by the so called flip angle:

$$\alpha(t) = \gamma B_1 t \tag{3.7}$$

By adjusting B_1 and t , any flip angle can be achieved. Maximum transverse magnetization is gained for $\alpha = 90$. For $\alpha = 180$ the initial longitudinal magnetization (before the RF pulse) is inverted. After the magnetization is tilted by the desired flip angle, the RF pulse is switched off. At this particular time all the spins precess perfectly in phase with the Larmor frequency of the static magnetic field. The evolution of the RF-modified orientation of the magnetization is discussed in the following section.

3.1.3 Relaxation Phenomena

Any deviation from the state of thermal equilibrium - such as the excitation of the spins in the static magnetic field by the RF pulse - forces the magnetization back towards the equilibrium state by exchange of energy between the spin ensemble and its surroundings. There are two such relaxation mechanisms occurring independently from each other:

- longitudinal relaxation, which originates from interactions between spins and their surroundings (spin-lattice), and
- transverse relaxation, which is caused by interactions among spins themselves and by inhomogeneities of the magnetic field.

As soon as the RF pulse starts to tilt the orientation of the aligned magnetization, longitudinal relaxation counteracts this, forcing the z-component M_z to relax to-

wards its initial value M_{z0} (before the excitation). The larger the change of the z-component of the magnetization is, the larger is the relaxation towards the equilibrium state:

$$\frac{dM_z}{dt} = \frac{M_{z0} - M_z}{T_1} \quad (3.8)$$

where T_1 is the characteristic time constant for longitudinal relaxation. From this the evolution of M_z can be described:

$$M_z(t) = M_{z0}(1 - e^{-\frac{t}{T_1}}) \quad (3.9)$$

The RF pulse initiates a transverse magnetization M_{xy0} , and causes all the spins to precess in phase. Due to transverse relaxation, the spins start to dephase over time as soon as the RF pulse is switched off. This decreases the net magnetization in the xy-plane. The decay of transversal magnetization occurs as a result of spin-spin interaction, and is characterized by the time constant T_2 . Additionally to spin-spin relaxation, there is another effect contributing to the decay of M_{xy0} . Inhomogeneities of the main magnetic field and varying magnetic properties within the tissue cause local variations of the effective magnetic field seen by the protons. This causes the precession frequencies of the spins to deviate from the Larmor frequency of the undisturbed static magnetic field. This range of precession frequencies causes additional dephasing of the spins as some precess faster or slower than others. In order to combine both transversal relaxation mechanisms, an effective time constant T_2^* is defined as:

$$\frac{1}{T_2^*} = \frac{1}{T_2} + \frac{1}{T_2'} \quad (3.10)$$

where T_2' is the time constant of the inhomogeneity-induced relaxation. Transverse relaxation causes an exponential decay of the magnetization in the xy-plane:

$$M_{xy}(t) = M_{xy0}e^{\frac{-t}{T_2^*}} \quad (3.11)$$

3.2 Magnetic Resonance Imaging

Imaging requires the MR signal from each part of the object to be assigned to the correct location. This necessitates a number of steps, in which the signals are spatially encoded by the application of linear magnetic gradient fields. Selectively exciting spins within one slice (z-position) in the object is followed by phase-encoding (y-position) and frequency-encoding (x-position). There are numerous sequences established for data acquisition, and the GE sequence is described in the following. The image, which is a representation of the transverse magnetization, is sampled in the frequency domain denoted as the k-space in which the position of the signals from each location are encoded. By Fourier-transforming the sampled k-space the image of the object is obtained.

3.2.1 Encoding

Slice Selection

Selective slice excitation is achieved by applying a gradient G_z together with the RF pulse. The gradient causes the precession frequency of the spins in the object to be a function of their z-position:

$$\omega(z) = \gamma(B_0 + G_z z) \quad (3.12)$$

i.e. spins from different slices precess at different frequencies. Therefore the RF pulse only affects spins of one particular slice which meets the resonance condition for excitation.

Phase Encoding

After slice excitation and rephasing of the spins, another gradient in y-direction G_y is applied for a certain period of time T_y before the readout process. This gradient causes the spins to acquire different phase increments according to their y-position:

$$\phi_p(y) = -\gamma G_y y T_y \quad (3.13)$$

The magnetization as a function of the gradient direction then reads as:

$$M_{xy}(y, T_y) = M_{z0}(y) e^{-i\gamma G_y y T_y} \quad (3.14)$$

For phase encoding, the whole sequence is repeated a number of times, each time using a modified G_y . Therefore the pattern of spin orientation is changed for every single repetition, each providing different information content to the image.

Frequency Encoding

During readout of the signal another gradient G_x is applied, which makes the precession frequencies a function of the location along the x-direction:

$$\omega(x) = \gamma(B_0 + G_x x) \quad (3.15)$$

Therefore magnetization along the frequency encoding direction can be written as:

$$M_{xy}(x) = M_{z0}(x)e^{-i\gamma G_x x t} \quad (3.16)$$

The received signal is therefore a composition of many different frequencies. By Fourier-transforming this, the contribution from spins at location x can be determined:

As G_x would dephase and therefore decrease the signal during readout, a negative gradient in x -direction is used before the readout process to deliberately dephase the spins prior to frequency encoding. G_x then inverts this dephasing, leading to a signal echo and high signal level in the middle of the readout process.

3.2.2 Image Formation

The signal originating from the excited slice is encoded by the use of gradients, and can be expressed for a single repetition, i.e. for one particular phase encoding gradient as:

$$S(t, G_y) = \int_{Slice} M_{xy}(x, y) e^{-i \int \omega(x, y, t) dt} dx dy \quad (3.17)$$

The whole sequence delivers a number of such signals $S(t, G_y)$. The phase of the signal from a particular location is described by:

$$\begin{aligned} \int \omega(x, y, t) dt &= \gamma x \int G_x(t) dt + \gamma y \int G_y(t) dt \\ &= \gamma x G_x t + \gamma y G_y T_y \\ &= k_x x + k_y y \end{aligned} \quad (3.18)$$

where the abbreviations k_x and k_y can be seen as some kind of standardized time scale. With this the measured signal can be rewritten as:

$$S(k_x, k_y) = \int_{\text{Slice}} M_{xy}(x, y) e^{-i(k_x x + k_y y)} dx dy \quad (3.19)$$

where S and M_{xy} constitute a Fourier pair, with k_x and k_y spanning the k-space. Therefore the received MR-signal is the Fourier-transform of the desired image, which is obtained by sampling the k-space. For each repetition of the sequence one line in k-space is sampled. Each G_y -value determines one particular k_y , and with G_x the spatial frequencies in x-direction from $-k_{max}$ to $+k_{max}$ are acquired for this line. Practically it is not possible to sample the k-space entirely, but only a subset of discrete points.

3.2.3 Gradient Echo Sequence

SWI uses the so called gradient echo (GE) sequence (Fig.6), which is described in the following. The GE sequence uses a gradient to deliberately cause spins to dephase before spins are refocused again by an inverted version of this gradient. The echo formed this way is weighted by the T_2^* decay, i.e. the signal is sensitive to magnetic field inhomogeneities arising from tissue susceptibility.

In 3D GE imaging a volume or slab of the object is excited by the RF pulse, rather than a single slice like in 2D imaging. The fundamental difference to a 2D sequence is the use of a second phase-encoding gradient to differentiate the signal along the excitation direction, acting as a slice-selection gradient. After each slab excitation, a number of different slice-selecting gradients are used to encode slices in the volume. For each slice phase- and frequency-encoding is done just like in a 2D-sequence. 3D GE imaging offers the advantage, that the profile of slices is indeed rectangular, meaning that an equal contribution to the signal comes from every proton in the slice. As a result of the rectangular magnetization profiles, imaging can be done

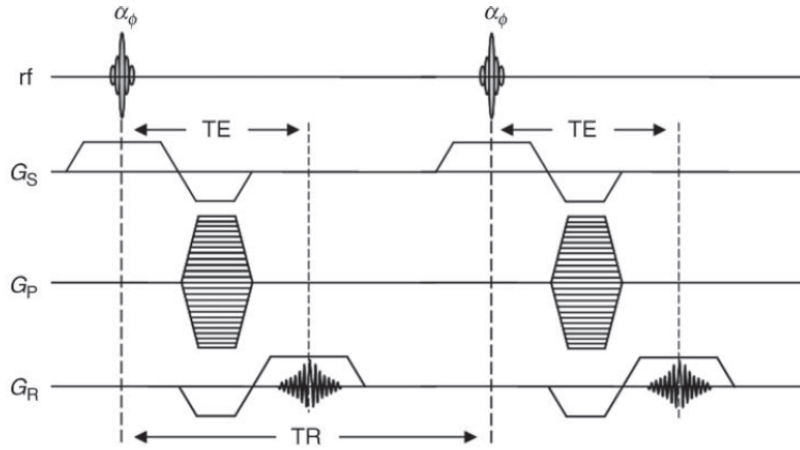


Figure 6: The Gradient Echo Sequence. The RF pulse (rf) excites the spins within a slice as the slice encoding gradient (G_S) is switched on. After excitation and for each repetition a certain phase encoding gradient (G_P) is switched on. The readout gradient (G_R) maps the location of spins along the x-axis, while the echo is formed after a time T_E . After a time T_R , the sequence is repeated (reproduced from Ref.[4]).

very effectively, since there is no cross-talk and therefore no need for gaps between consecutive slices. The 3D approach therefore exceeds the SNR of 2D imaging when the number of slices is high. One disadvantage of 3D imaging is that it requires longer acquisition times, since an additional phase-encoding gradient has to be applied for each slice. In order to provide acceptable acquisition times though, short repetition times (T_R) and low flip angles (15-25 degrees) are used, which results in a low specific absorption ratio (SAR) i.e. the RF power deposition in an object. 3D sequences also require a more time-consuming image reconstruction since a full 3D Fourier-transformation has to be performed on the measured k-space data. Nevertheless, the good coverage of volumes and the high SNR makes 3D GE imaging best suitable for SWI, especially when even very small vessels should be visualized.

3.3 Imaging with Phased Array RF Coils

To transmit the excitation pulse and to receive the MR signal, so called RF coils are used. The measured output of a coil l depends on both the magnitude and the direction of the RF excitation pulse, and is proportional to:

$$U_l(t) = \omega MV B_{t,l} \cos(\omega t - \theta_l + \psi) \quad (3.20)$$

where V is the voxel volume, M is the spin density, $B_{t,l}$ is the magnitude of the RF pulse, ψ is an arbitrary phase of the magnetization vector and θ_l represents the direction of the RF pulse. There are different coil systems used in MRI today. Volume coils, which use a single RF coil enclosing the object being imaged, single surface coils and phased array RF coils. Phased array RF coils consist of a multitude of small coils closely positioned around the surface of the object. Volume coils provide homogenous RF excitation and sensitivity over a large volume, whereas the small surface coils in a phased array are characterized by highly inhomogeneous RF excitation and high sensitivity close to the surface.

Phased array coils provide two important advantages over volume coils. First, the SNR is higher for small surface coils than for volume coils. Second, the parallel use of multiple receive coils (parallel imaging) allows for a reduction in scan time, since the spatially varying coil sensitivities have an encoding effect complementary to the encoding by field gradients, which can be used to reduce the number of phase encoding steps in the acquisition. Image formation from such sensitivity encoded data is well established (SENSE [5], GRAPPA [6]), and widely used.

Roemer et al. [7] were the first to comprehensively describe the use of a phased array for MRI. They showed that parallel imaging requires decoupling of the coils in order to acquire data simultaneously and separately with each element in the array, eliminating mutual inductances. Decoupling is achieved by overlapping adjacent coils, and attaching low input impedance preamplifiers to all coils. They also demonstrated that for optimum SNR and artefact suppression, multiple coil data should be combined by weighting the signal from each coil by the sensitivity of that coil for each voxel. The signal at a voxel position from a single coil l in an array of N_c coils can be written as:

$$s_l = \rho b_l + \eta_l \quad (3.21)$$

where ρ is the MR-signal from the object, b_l is the coil sensitivity and η_l is the noise from the coil. The reconstruction process can be modeled with a $N_c \times 1$ complex filter vector \mathbf{m} which is used to coherently sum the individual complex coil images described by the $N_c \times 1$ vector \mathbf{s} to form a composite image:

$$S = \mathbf{m}^* \cdot \mathbf{s} = \sum_{l=1}^{N_c} m_l^* \cdot s_l \quad (3.22)$$

For optimum reconstruction, i.e. maximum SNR in the composite image, the filter vector is the so called spatial matched filter [7] which is computed for each voxel by:

$$\mathbf{m} = \mathbf{R}_\eta^{-1} \mathbf{b} \quad (3.23)$$

where the complex vector \mathbf{b} describes the magnitude and phase of the transverse magnetic field from each coil at the voxel position and \mathbf{R}_η^{-1} is the array noise correlation matrix. Whereas noise correlation for multiple coils can be measured with a noise calibration scan, obtaining detailed knowledge about the coil sensitivities b_l requires a reference scan with a volume coil, which is not integrated in most high- and UHF systems.

Therefore, Roemer et al. [7] proposed a suboptimal coil combination approach known as sum-of-squares (SOS), which uses complex coil signals as estimates for the respective coil sensitivities. The SOS reconstruction ignores noise correlation among coils and reduces to the square root of the sum over the squared magnitude images from individual coils:

$$S_{SOS} = \sqrt{\sum_l^{N_c} |s_l|^2} \quad (3.24)$$

The simplistic SOS reconstruction does not require knowledge of coil sensitivities, but suffers from poor SNR in regions of low signal and enhances motion and flow artefacts. The method is adequate for reconstructing magnitude images, but fails to generate reliable composite phase images.

Reconstructing phase from multiple coils is complicated by two problems. First, object phase information from each coil is superimposed by a specific and spatially varying receiver offset, which constitutes the time-independent part of the measured phase:

$$\phi_l(\vec{r}, T_E) = \Delta\phi(\vec{r}, T_E) + \theta(\vec{r})_{R,l} = 2\pi\gamma\Delta B_0 T_E + \theta(\vec{r})_{R,l} \quad (3.25)$$

where ϕ_l is the measured phase from coil l for an echo time of T_E , $\Delta\phi$ is the object phase information arising from local inhomogeneities of the main magnetic field ΔB_0 and $\theta_{R,l}$ is the coil-specific phase offset (Fig.7).

Second, the limited encoding range for phase of $[0, 2\pi]$ leads to discontinuities of 2π , which are present in the image as isocontours known as wraps (Fig.8). Both, receiver phase offsets and wraps lead to interferences and signal cancellation in reconstruction when complex data is summed over coils or when phase from each coil is magnitude weighted and then summed over coils.

There has been increasing interest in methods that employ the phase part of the MR-signal over the past decade. Phase imaging, susceptibility weighted imaging [1] and susceptibility mapping [8] are widely used for imaging the venous vasculature and iron storage, and are constantly refined. Increased susceptibility effects at high field make these especially suitable for the use in ultra high field (UHF) imaging,

which has required the development of methods which reconstruct multiple coil data reliably without the need for volume reference scans and generate high-quality composite phase images.

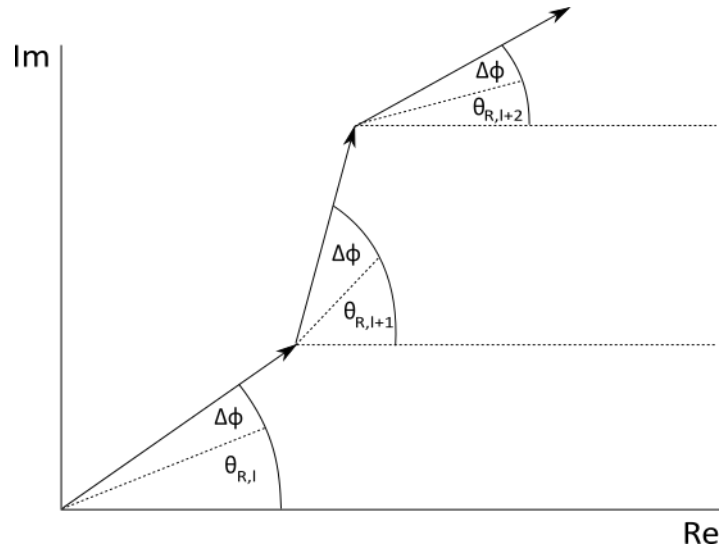


Figure 7: Complex vectors represent the signal from three coils l , $l+1$ and $l+2$. The phase part of each complex vector consists of the object phase $\Delta\phi$ and a coil-specific phase offset θ_R .

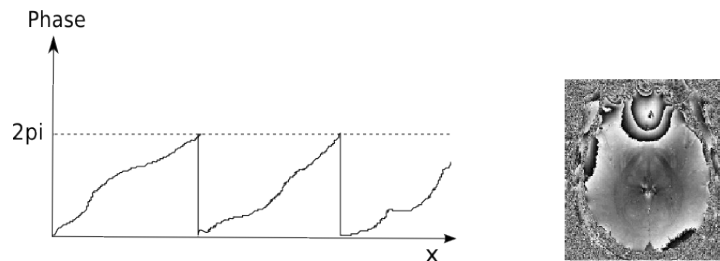


Figure 8: The limited encoding range for phase leads to discontinuities of 2π (left), which are present in the image as isocontours (right). The right image shows the measured phase of a brain.

3.3.1 Phase in MRI

The RF signal frequency received by the MR scanner is close to the Larmor frequency of the main magnetic field ω_0 , and is demodulated to yield the deviations from the main magnetic field. The resulting signal constitutes a complex vector which represents the transverse component of the magnetic moment in a rotating frame of

frequency ω_0 . The measured signal from a coil l in a phased array is described by:

$$S_l(\vec{r}, T_E) = M_l(\vec{r}, T_E) \cdot e^{i\phi_{w,l}(\vec{r}, T_E)} \quad (3.26)$$

Where M_l is the magnitude and $\phi_{w,l}$ is the measured wrapped phase of the signal. The dependence of the magnitude on T_E arises from progressing decay of transverse magnetization by T_2^* -relaxation. For a given echo time T_E , the phase of the MR-signal is given by:

$$\phi_{w,l} = \Delta\phi(\vec{r}) + \theta_{R,l}(\vec{r}) + \eta_{R,l} \quad (3.27)$$

where $\Delta\phi(\vec{r})$ is the interesting object phase information, $\theta_{R,l}(\vec{r})$ is the coil-specific receiver phase offset and $\eta_{R,l}$ denotes the noise in the coil, which is not considered in the following discussion for the sake of simplicity. In order to obtain the real range of phase information, $\phi_{w,l}$ has to be unwrapped, which corresponds to adding integer multiples of 2π at the right positions:

$$\phi_l(\vec{r}) = \phi_{w,l}(\vec{r}) + 2\pi \cdot n(\vec{r}) \quad (3.28)$$

where $\phi_l(\vec{r})$ is the unwrapped phase, and $n(\vec{r})$ is an integer multiple. Additionally, the coil-specific receiver phase offset has to be removed in order to obtain the interesting part of the phase information which reflects magnetic field inhomogeneity:

$$\Delta\phi(\vec{r}) = 2\pi \gamma \Delta B_0(\vec{r}) T_E \quad (3.29)$$

where ΔB_0 is the sum of two distinct field variations:

$$\Delta B_0(\vec{r}) = \Delta B_{loc}(\vec{r}) + \Delta B_{back}(\vec{r}) \quad (3.30)$$

where ΔB_{loc} is the local variation caused by tissue susceptibility, and ΔB_{back} is the background field variation arising from global geometry, air-tissue interfaces or other inhomogeneities. For the purpose of SWI, only ΔB_{loc} is of interest. Due to the non-local field perturbations induced by the susceptibility distribution, ΔB_{loc} and susceptibility are related via a response function:

$$\Delta B_{loc}(\vec{r}) = B_0 \cdot \chi(\vec{r}) \otimes G(\vec{r}) \quad (3.31)$$

where \otimes denotes a convolution, χ is the susceptibility distribution and G is the point dipole response function which describes the effect of a susceptibility source on the magnetic field and is given by:

$$G(\vec{r}) = \frac{1}{4\pi} \frac{3\cos(\theta)^2 - 1}{r^3} \quad (3.32)$$

where θ is the angle between the susceptibility source (i.e. the axis of a cylindrical vein f.e.) and the main magnetic field. This means, that although the phase of the MR signal is sensitive to the local field variations generated by the susceptibility distribution, it can be distant to the source. Moreover, ΔB_{loc} depends on the geometry and orientation of the susceptibility source, which makes it difficult to obtain accurate knowledge about an objects' susceptibility distribution from phase information. However, there has been a rapid development of methods which recover susceptibility from phase information by solving Eq.(3.31) for χ - a concept known

as quantitative susceptibility mapping (QSM) [9, 10, 11].

4 Theory

4.1 Reconstructing Multiple Coil Data

The need for reliable combination of multiple coil phase images has increased drastically over the past years with the increased use of phased array coils at ultra high magnetic field. Combining phase images from a phased array is challenging for two reasons which were already introduced in section 3.3 and are shortly repeated in the following. First, the limited encoding range causes discontinuities of 2π in the phase images known as wraps. Second, phase information from each coil is subject to a spatially varying receiver offset, i.e. the time-independent part of the phase information:

$$\phi_l(\vec{r}, T_E) = 2\pi\gamma\Delta B_0 T_E + \theta(\vec{r})_{R,l} \quad (4.1)$$

where $\phi_l(\vec{r}, T_E)$ is the measured phase information from coil l , $\theta(\vec{r})_{R,l}$ is the receiver phase offset in that coil, T_E is the echo time and ΔB_0 is the deviation from the main magnetic field. Correcting the phase information from each coil for the specific receiver offset is vital in order to reliably sum separate phase images from the multitude of coils in a phased array.

Coil-specific phase offsets can be measured or estimated and removed from each coil in the phased array prior to combining individual phase images (sections 4.1.2 - 4.1.4). Unwrapping phase images can be done using sophisticated algorithms (section 4.2). The simplistic Homodyne Filter approach (section 4.1.1) achieves both offset removal and unwrapping of phase images by high-pass filtering complex coil signals. The following sections give an introduction to the approaches implemented

or tested in this work.

4.1.1 Homodyne Filter

The most common method to remove offsets and unwrap phase images from multiple coils is to high-pass filter each phase image [12], before these are summed over all coils by the weighted mean approach [13]. High-pass filtering of phase images can be achieved by dividing the measured complex signal $S_l = M_l e^{i\phi_l}$ from each coil by a smoothed version of the same data. Smoothing is performed by convolving the complex signal with a low-pass filter in image space:

$$S_l^{LP} = S_l \otimes LP \quad (4.2)$$

where LP represents the low-pass filter. This smoothed version is then divided into the original complex signal from coil l which yields a high-pass filtered complex coil signal:

$$S_l^{HP} = \frac{S_l}{S_l^{LP}} = \frac{M_l}{M_l^{LP}} \cdot e^{i(\phi_l - \phi_l^{LP})} \quad (4.3)$$

where HP stands for high-pass filtered. Taking the angle of this high-pass filtered complex coil signal provides a high-pass filtered version of the measured phase map from coil l due to the subtraction of slow variations in phase ϕ_l^{LP} :

$$\phi_l^{HP} = \text{angle}(S_l^{HP}) = \phi_l - \phi_l^{LP} \quad (4.4)$$

The degree of high-pass filtering depends on the size of the low-pass filter for smoothing. This is best explained using k-space formalism and the fact that a convolution

in image space corresponds to a simple multiplication in Fourier space. Knowing this, it becomes obvious that smoothing complex data with a filter increases low frequency k-space constituents within the range of the filter size. Decreasing the width of the low-pass filter in image space, i.e. increasing the width in Fourier space, expands the affected k-space range to higher frequencies. Thus narrowing the filter width in image space high-pass filters data more strongly due to removing the smoothed version by complex division. Filtering phase images suppresses receiver offsets and wraps, which allows for coil combination by the weighted mean approach:

$$\phi_{comb} = \frac{\sum_l M_l \phi_l^{HP}}{\sum_l M_l} \quad (4.5)$$

where ϕ_{comb} denotes the combined phase information from all coils. It is well known that the method is prone to error as described in Ref.[14], and demands excessive high-pass filtering for removing phase wraps sufficiently, which can lead to artefacts and loss of low frequency information. Therefore, the Homodyne filter approach represents a trade-off between unwrapping the phase and conserving image information.

4.1.2 Multiple Coil Phase Combination with Constant Offsets (MCPC-C)

It is well known that receiver phase offsets vary spatially over the FOV, i.e. $\theta_{R,l} = \theta_{R,l}(\vec{r})$. The simplistic MCPC-C approach [13] assumes these to be constant throughout the image and can be estimated from individual phase images by taking the phase value from the centre voxel, or by averaging phase values within a region around the centre voxel, if in the centre of the FOV there is sufficient signal in all detectors:

$$\theta_{R,l}^{est} = \phi(\vec{r}_{centre}) \quad (4.6)$$

where $\theta_{R,l}^{est}$ is an estimation of the spatially varying receiver phase offset of coil l and $\phi(\vec{r}_{centre})$ is the phase value at the centre voxel. The estimated receiver offsets are subtracted from each phase image, setting the phase from all coils to zero at the point of correction, i.e. the centre voxel. The phase-corrected complex data is then combined by the sum over all coils. Taking the angle of this sum yields a combined phase image:

$$\phi_{comb} = \text{angle}\left(\sum_l M_l e^{i(\phi_l - \theta_{R,l}^{est})}\right) \quad (4.7)$$

where ϕ_{comb} is the combined phase information, l represents a coil, M_l is the magnitude information from coil l and ϕ_l is the original measured phase.

4.1.3 Virtual Reference Coil Approach (VRC)

In B0 mapping [15, 16] and phase contrast imaging, two images are acquired at different echo times according to Eq.(4.1). The phase difference between the two echoes is the tissue phase evolution during the time-offset between the two acquisitions and contains important clinical information. The optimum estimate for the phase difference between two complex images (P1,P2) was investigated in Ref.[17] and can be described by:

$$\Delta\phi = \text{angle}(P^2 \cdot P^{1*}) \quad (4.8)$$

When the images are acquired using a phased array coil, P^1 and P^2 have to be combined from multiple coil data first, before phase difference can be calculated. Optimum reconstruction of phase images however, requires coil sensitivities to be known. When coil sensitivities are not known, phase difference can be calculated from individual complex coil signals according to Ref. [7] via:

$$\Delta\phi_{comb} = \text{angle}\left(\sum_{l,q=1}^{N_c} p_l^2 \cdot \frac{1}{\lambda} R_{l,q}^{-1} \cdot p_q^{1*}\right) \quad (4.9)$$

where p_q^1 and p_l^2 are the individual complex coil measurements from the first and the second echo, $R_{l,q}$ is the noise covariance matrix for the coils and λ is a scaling factor.

Parker et al. [18] established a similar method to obtain an estimate of the absolute object phase from a single-echo phased array measurement. This is achieved by matching individual coil phase information to a virtual reference coil (VRC). The phase of the object is then derived from the phase difference between the original and the phase-referenced coil measurements using eq.(4.9). When the array of coils contains a reference coil r which is sensitive over the entire image, the difference in phase between this reference coil and the k th coil is given by:

$$e^{i\Delta\phi_{rk}} = e^{i\phi_r} e^{-i\phi_k} = e^{i(\theta_r - \theta_k + \eta_r - \eta_k)} \quad (4.10)$$

Where ϕ_r and η_r is the phase and the noise of the reference coil, ϕ_k and η_k is the phase and the noise of the k th coil and θ_r and θ_k are the receiver phase offsets from both coils. Applying a low pass filter on this phase difference suppresses noise, but leaves the slowly varying difference in coil phase unaffected:

$$\langle e^{i\Delta\phi_{rk}} \rangle = e^{i(\theta_r - \theta_k)} \quad (4.11)$$

This filtered phase difference can be used to replace the receiver phase offset from coil k by the offset from the reference coil:

$$e^{i\hat{\phi}_k} = e^{i(\theta_k + \phi + \eta_k)} e^{i(\theta_r - \theta_k)} = e^{i(\theta_r + \phi + \eta_k)} \quad (4.12)$$

which is then combined with the original measurement from coil k:

$$\hat{p}_k = p_k e^{i\hat{\phi}_k} \quad (4.13)$$

Phase referencing as described in eq.(4.10) - eq.(4.13), can be done equivalently for all other coils in the phased array. The modified coil measurements in the form of eq.(4.13) are then substituted into eq.(4.9), which yields a combined phase difference between the original coil measurements and the measurements referenced to the virtual coil:

$$\Delta\phi_{comb} = \theta_r + \phi + \text{angle}\left(\sum_{l,k=1}^{N_c} p_l \cdot \frac{1}{\lambda} R_{l,k}^{-1} \cdot p_k^* e^{i\eta_k}\right) \quad (4.14)$$

where ϕ is the object phase. Because the noise term $e^{i\eta_k}$ is small, the last term in eq.(4.14) is just the sum-of-squares (SOS) of the original coil measurements, which has negligible phase.

Phase referencing necessitates a coil which is sensitive over the whole object. In parallel imaging at high field, none of the multiple coils achieves full FOV - coverage

and there is no volume reference coil available. Parker et al. (ref.Parker) established a so called virtual reference coil, which is obtained from a linear combination of the coil measurements:

$$v = \sum_{l=1}^{N_c} w_l p_l = \sum_{l=1}^{N_c} |w_l| e^{i\phi_{ref,l}} e^{i(\theta_l + \phi + \eta_l)} \quad (4.15)$$

where the weights w_l are calculated from the original coil measurements:

$$w_l = \frac{|p_l| e^{-i\phi_{ref,l}}}{\sum_k |p_k|} \quad (4.16)$$

Where the magnitude part of w_l assures weighting of coils with high SNR at the respective voxel positions, and the phase part $e^{-i\phi_{ref,l}}$ minimizes variation in phase among coils, where $\phi_{ref,l}$ can be obtained from taking the phase value at the centre of the phase images according to Hammond et al. [13].

4.1.4 Using Phase Offsets From a Short Reference Scan (COMPOSER)

In principle there is no possibility to obtain accurate maps of receiver phase offsets for each coil in a phased array when there is no volume reference coil available. The COMPOSER approach [19] however, derives estimates for the offsets for each coil using a reference scan of very short echo-time. These are used to compensate the phase offsets in the acquired data of interest (target scan). Fig.9 shows the concept of the COMPOSER approach.

When echo time is sufficiently short, phase information approximates to the coil-specific offsets as time-dependent contributions to phase are yet negligibly small (see Eq.(4.1)). This can be utilized by a low resolution scan of very short echo time, for which the measured phase can be written as:

$$\phi_{ref,l}^{low} = \theta_{R,l}^{low} \quad (4.17)$$

where $\phi_{ref,l}^{low}$ denotes the measured phase of the l th coil from the low-resolution reference scan, and $\theta_{R,l}^{low}$ represents a low-resolution version of the phase offset of coil l . In order to remove these estimates from target phase images, low-resolution reference data has to be upsampled to fit the resolution of the target scan. Upscaled reference data is then complex divided into target data, which subtracts the offset estimates from target phase information from each coil:

$$\phi_{corr,l} = \text{angle}\left(\frac{S_{target,l}}{S_{ref,l}}\right) = \phi_{target,l} - \phi_{ref,l} = \phi_{target,l} - \theta_{R,l} \quad (4.18)$$

where $\phi_{corr,l}$ is the corrected target phase information from coil l and $\phi_{ref,l}$ and $\theta_{R,l}$ is the upsampled reference phase information, i.e the high-resolution estimate of the phase offset of coil l . The combined phase image for the target data is then obtained by taking the angle of the sum over all phase-corrected complex coil signals:

$$\phi_{comb} = \text{angle}\left(\sum_l M_l e^{i\phi_{corr,l}}\right) \quad (4.19)$$

4.1.5 The Adaptive Combine Approach

The adaptive reconstruction approach [21] uses a stochastic formulation of the spatial matched filter, in which signal and noise processes are represented via array correlation matrices. These are estimated from the individual coil images by averaging complex cross products over local regions in the FOV. Finally, the optimum reconstruction vector \mathbf{m} is obtained from eigenanalysis of the correlation matrices.

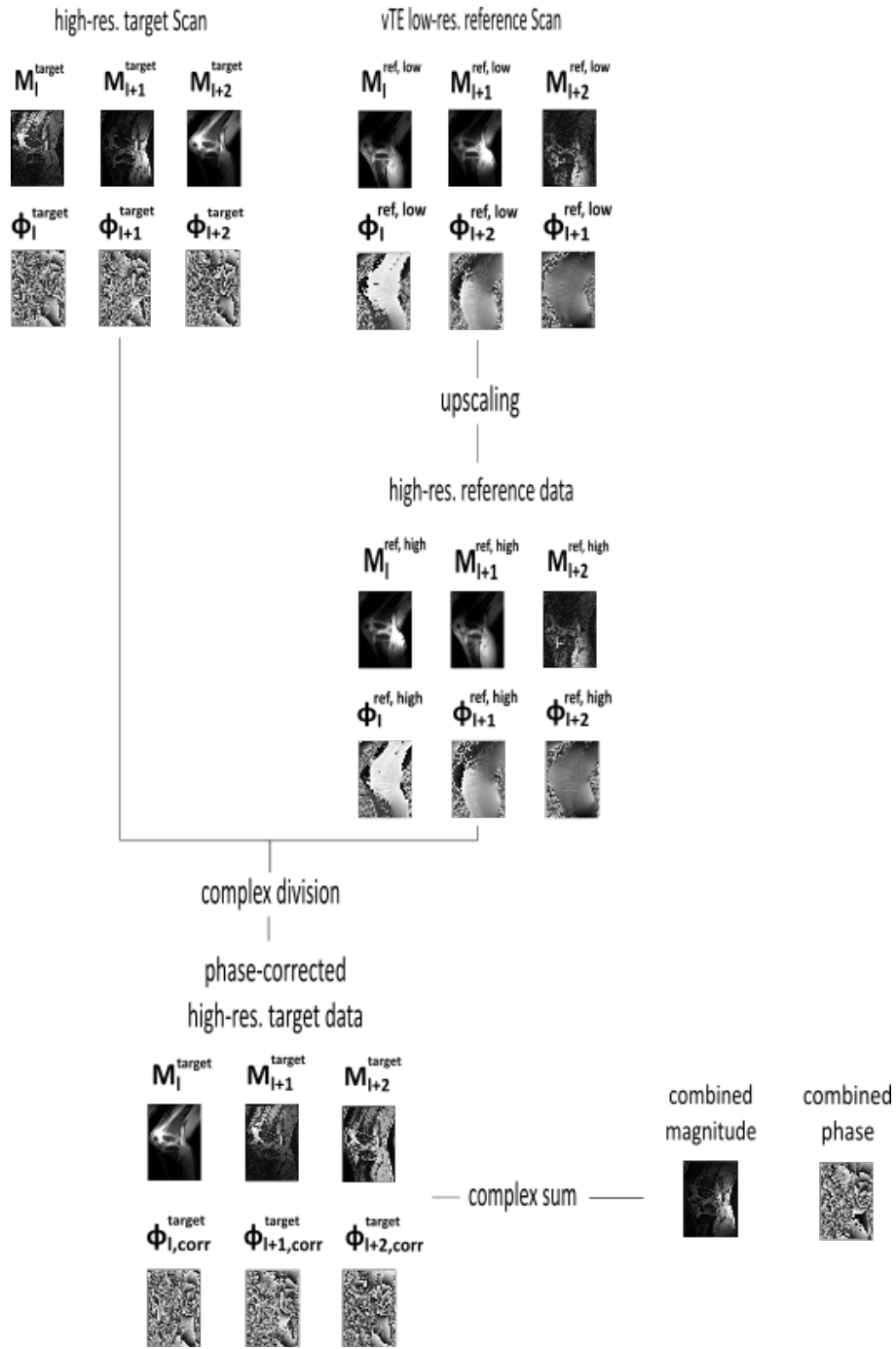


Figure 9: Workflow for the coil combination with the COMPOSER approach shown for three coils $l, l + 1, l + 2$. Additionally to the acquired data (target scan), a low-resolution reference scan with a short, variable echo time is acquired (vTE reference scan [20]), which has to be upscaled to the target scan resolution, before phase offsets are removed from coils by complex division to yield phase corrected target scan data which is then combined by summing complex coil signals.

The stochastic formulation describes the signal from the object by the desired signal $s(t)$ and a noise part $n(t)$. The measured signal and noise from the j th coil are denoted by $s_j(t)$ and $n_j(t)$ and the array correlation matrices for both signal and noise processes are given by:

$$R_s(j, k) = E[s_j \cdot s_k^*] \quad \text{for } j, k = 1, \dots, N_c \quad (4.20)$$

$$R_n(j, k) = E[n_j \cdot n_k^*] \quad \text{for } j, k = 1, \dots, N_c \quad (4.21)$$

Where E denotes the expectation evaluated over time. The filter vector which maximizes the SNR in the complex composite image is the eigenvector of the matrix product:

$$P = R_n \cdot R_s \quad (4.22)$$

having the maximum corresponding eigenvalue [22]. The stochastic formulation of the matched filter can be transferred to phased array imaging by replacing time averaging in Eq.(4.21) by averaging complex coil signal cross products over 2D regions:

$$\hat{R}_s = \sum_{(x,y) \in \text{roi}} s_j(x, y) \cdot s_k^*(x, y) \quad \text{for } j, k = 1, \dots, N_c \quad (4.23)$$

Where roi denotes a region in the FOV. The array correlation matrix for noise R_n is either assumed to equal the identity matrix or is estimated from a noise calibration scan. With that, the matched filter is calculated according to the eigenanalysis of the matrix product in Eq.(4.22).

4.2 Phase Unwrapping

4.2.1 Spatial Unwrapping

Several approaches exist that unwrap phase directly in the image domain. Starting from a seed voxel, neighbouring voxels or regions of voxels are unwrapped and merged together based on a phase-difference cost-function (PRELUDE [23]) or predictions of phase values (PHUN [24]). Noise is likely to corrupt this process and errors resulting from this propagate throughout the image due to region-merging. A method established by Cusack et al. [25] tackles the problem associated with noise by calculating a noise estimator field and guiding unwrapping around noisy regions. In the following, the PRELUDE algorithm is introduced as a representative for spatial unwrapping approaches.

4.2.2 PRELUDE Unwrapping

“PRELUDE” (Phase Region Expanding Labeller for Unwrapping Discrete Estimates) uses a region-merging approach based on a cost function, that penalises phase differences across boundaries.

The method divides the whole phase image into N single entities, in such a way that none of them contains phase wraps. Therefore, the integer n to be found for unwrapping is the same for all voxels in a single entity (region A e.g.):

$$\phi_{Aj} = \phi_{measured,Aj} + 2\pi n_A \quad (4.24)$$

where ϕ_{Aj} is the true (unwrapped) phase in that region in voxel j , and $\phi_{measured,Aj}$ is the corresponding measured phase. The cost function sums up all squared differences between neighbouring voxels at the interface of two regions. By differentiating this cost function with respect to the individual parameters between two interfaces and setting this to zero, $N-1$ equations for the minimum cost solution are obtained.

In order to find the set of solutions which yield the minimum total cost for the whole image, the “Region-merging algorithm” observes the behavior of difference in the total cost between a locally best solution and a suboptimal solution. By determining the maximum of this cost difference, the algorithm searches for the interface where “getting the offset wrong” is the most disastrous. The voxels of this interface are then unwrapped using the optimal solution and merged together to a new entity. Following this, the cost function is updated for this new image and the algorithm performs the next iteration. Therefore, the algorithm merges all entities in a pairwise manner, finally creating one single entity, namely the unwrapped phase image.

4.2.3 Fourier-Based Unwrapping

A concept for unwrapping phase images is to calculate the difference between adjacent pixels and to take the positions where this exceeds a certain threshold value as a wrap. This amounts to taking the first order partial derivative of the wrapped phase. Though wraps can be identified this way, a map of integer values $n(\vec{r})$ for obtaining the true unwrapped phase remains to be derived from that. Schofield and Zhu [26] established a method which obtains $n(\vec{r})$ directly from the wrapped phase, which is shown in the following.

The true unwrapped phase can be written as:

$$\phi(\vec{r}) = \phi_w(\vec{r}) + 2\pi n(\vec{r}) \quad (4.25)$$

where ϕ is the true and ϕ_w is the wrapped measured phase. The underlying concept is to apply the Laplace operator to Eq.(4.25) and solving for n :

$$n(\vec{r}) = \frac{1}{2\pi} \nabla^{-2} [\nabla^2 \phi(\vec{r}) - \nabla^2 \phi_w(\vec{r})] \quad (4.26)$$

where ∇^2 and ∇^{-2} are the forward and inverse Laplacian operators. The only unknown in Eq.(4.26) is the Laplace of the true phase $\nabla^2\phi$, which can be substituted by a relation between the true and the measured phase established in Ref.[27]:

$$\nabla^2\phi = \cos(\phi_w)[\nabla^2\sin(\phi_w)] - \sin(\phi_w)[\nabla^2\cos(\phi_w)] \quad (4.27)$$

Using fast Fourier techniques for the Laplacian operators according to Ref.[28] in Eq.(4.26) minimizes the influence of image noise and decreases computation time. Forward and inverse Laplacian operators in Fourier space are given by:

$$\nabla^2 f(x, y, z) = -\frac{4\pi^2}{N^2} FFT^{-1}\{(k^2 + l^2 + m^2)FFT[f(x, y, z)]\} \quad (4.28)$$

$$\nabla^{-2} g(x, y, z) = -\frac{N^2}{4\pi^2} FFT^{-1} \left\{ \frac{FFT[g(x, y, z)]}{(k^2 + l^2 + m^2)} \right\} \quad (4.29)$$

where (x, y, z) and (k, l, m) denote real- and Fourier-space voxel coordinates, FFT is the fast Fourier transform operation and FFT^{-1} is its inverse, and N is the number of pixels in the image.

The solution to eq.(4.26) is unique once boundary conditions are imposed along with the constraint that $n(\vec{r})$ can only be integers. The latter constraint can be realized simply by rounding the solution.

Calculating the Laplacians by using FFTs imposes periodic boundary conditions on $n(\vec{r})$ which do not generally hold true. Since the solution are integers, a more realistic constraint is that the gradient of $n(\vec{r})$ normal to the image boundary vanishes. This constraint can be imposed by using a symmetrized $2N \times 2N$ version of the measured wrapped phase which is generated from mirror reflection of the original $N \times N$ image as shown in Ref.[29]. The $2N \times 2N$ solution of eq.(4.26) obtained with this reflects the same mirror symmetry and the solution for the original input image can be derived therefore by extracting the original quadrant.

The image extension for emulating the condition of a vanishing normal gradient comes along with increased computation and memory demands.

Bagher-Ebadian et al. [30] showed that for conditions typical in MRI, i.e. objects are centrally located in the FOV, symmetric image extension in real space can be replaced by demodulating and mirroring the signal in Fourier space which works with the original image dimension size $N \times N$.

Once phase data from the multiple coils of a phased array has been combined and unwrapped, it can be used for the purpose of SWI, which is discussed in the following section.

4.3 Susceptibility Weighted Imaging

The phase part of the MR signal is sensitive to susceptibility, which can be used to increase the contrast for veins and tissues of different susceptibility in the magnitude image. A susceptibility weighted image (SWI) is generated by multiplying a phase mask by the magnitude image a number of times. The mask is created from rescaling a high-pass filtered version of the phase information. High-pass filtering prior to rescaling is necessary in order to weight phase changes rather than absolute phase values. This emphasizes small structures of high susceptibility (i.e. venous vessels) and interfaces between tissues of varying susceptibility in the magnitude by application of the mask. Contrast in the SWI result can be further enhanced by a minimum intensity projection (mIP) through slices, which increases the visibility of veins and their connectivity. The SWI processing steps are shown in Fig.11.

The most common form of a mask is shown in Fig.10. In order to weight positive phase changes, phase values < 0 are set to unity and phase values > 0 are scaled linearly from 1 to 0. Therefore each multiplication by the mask reduces the signal in voxels with positive phase values, which increases contrast in the magnitude image. However, this also increases the amount of noise in the rest of the magnitude image. Haacke et al. [1] investigated this relationship and searched for the number of mask

multiplications that should take place in order to yield maximum contrast to noise ratio (CNR) in the resulting SWI image. They found that in the brain CNR reaches a peak between 3-5 mask multiplications. In order to further enhance contrast in the SWI image, a minimum intensity projection (mIP) is performed.

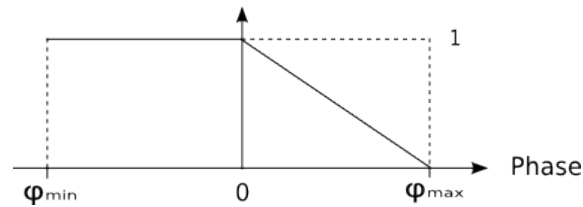


Figure 10: Positive phase mask.

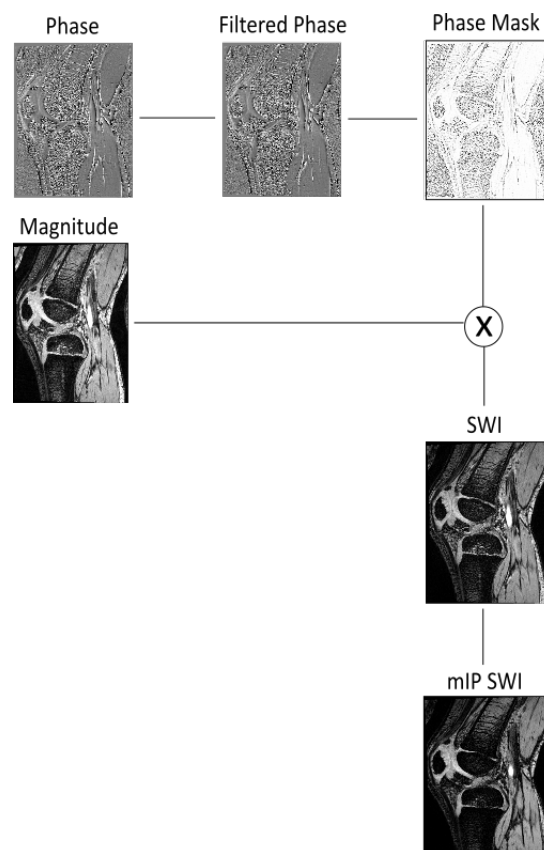


Figure 11: SWI processing scheme. Phase information is high-pass filtered, rescaled to a mask and then multiplied by the magnitude image. Finally a mIP is performed on the SW image.

4.4 Quantitative Susceptibility Mapping

Susceptibility maps can be obtained from phase by solving the inverse problem in Eq.(3.31), which can be expressed using the convolution theorem in the Fourier-space:

$$\Delta B(\vec{r}) = B_0 \cdot FT^{-1}[G(\vec{k})FT\chi(\vec{r})] \quad (4.30)$$

where $\chi(\vec{k})$ and $G(\vec{k})$ are the Fourier transforms of the susceptibility distribution and the point dipole response function respectively, and FT^{-1} denotes the inverse Fourier transformation. $G(\vec{k})$ is given by:

$$G(\vec{k}) = \begin{cases} \frac{1}{3} - \frac{k_z^2}{k^2} & \text{for } k \neq 0 \\ 0 & \text{for } k = 0 \end{cases}$$

Due to the zeros in G along the magic angles some spatial frequencies are under-sampled, i.e. the inversion process is ill-posed. This leads to streaking artefacts in the reconstructed susceptibility distribution. Therefore the inversion process is improved by incorporating regularization such as the total variation (TV):

$$\chi = \operatorname{argmin}_{\chi} \|\Delta B - B_0 \cdot FT^{-1}[G(\vec{k})FT\chi(\vec{r})]\|_2^2 + \lambda \|\nabla\chi\|_1 \quad (4.31)$$

where λ weights the TV-regularization term $\|\nabla\chi\|_1$, which leads to a smoother solution for the susceptibility distribution, i.e. streaking artefacts are reduced.

The use of accurate susceptibility maps for SWI can be advantageous, especially when non-local phase variations such as the dipolar appearance of veins (see Fig.12(middle)) is strong, i.e. at high field strength. Additionally, geometry and orientation dependencies of phase information from bulk susceptibilities are reduced in the SWI image,

when susceptibility itself is employed as the contrast information. Fig.12 shows the concept and the advantage of QSM for the resolution of the doubling artefact seen in veins.

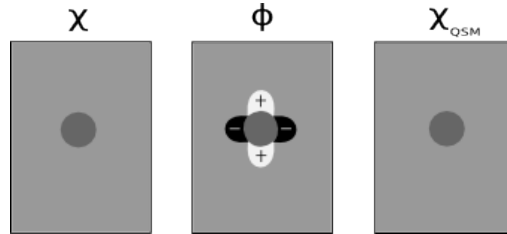


Figure 12: Illustrating the purpose of QSM. The susceptibility distribution shown (left) leads to positive and negative shifts in the phase (middle), which leads to the so called blooming artefact in SWI. QSM recovers the true susceptibility distribution from the phase (right) by solving the inverse problem.

4.5 True SWI

True SWI (tSWI) [31] denotes a concept which is equivalent to SWI beside the fact that instead of phase, the susceptibility information obtained with QSM is used as the source of contrast for visualizing structures of high susceptibility. The advantages of this modified SWI approach lies in the prevention of blooming and doubling artefacts seen in the conventional SWI approach. Therefore, tSWI improves vein visualization at the cost of calculating a QSM from the measured phase information. The creation of the mask (Fig.13) and the processing steps (Fig.14) in tSWI are equivalent to SWI, with susceptibility in lieu of phase.

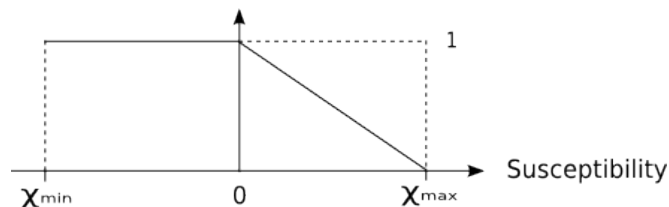


Figure 13: Positive susceptibility mask.

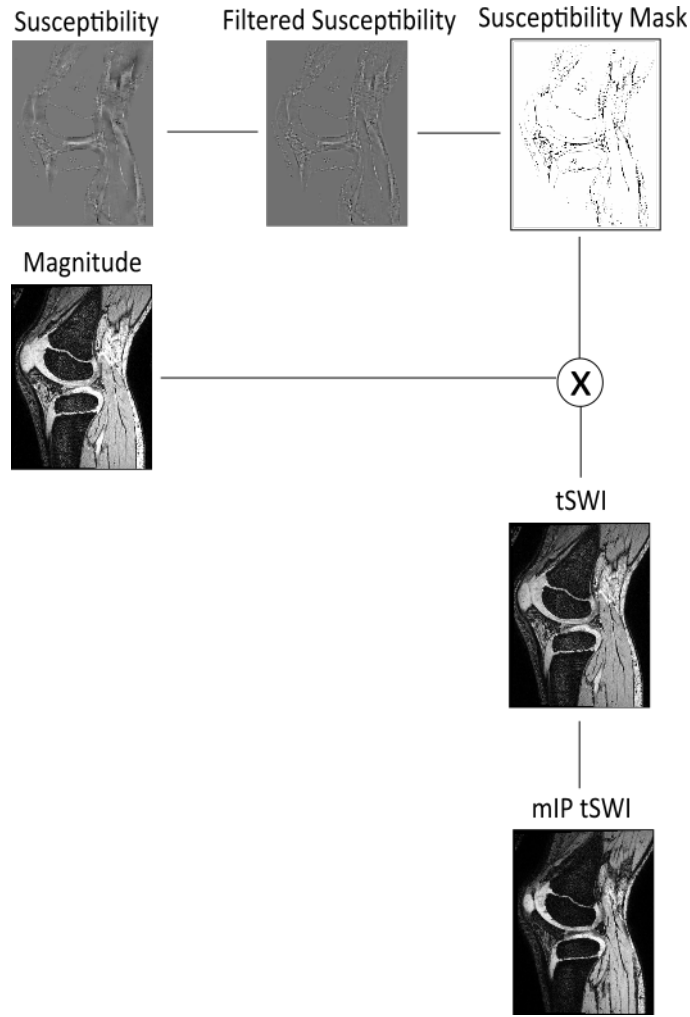


Figure 14: Processing scheme for tSWI.

5 Materials and Methods

For this work a GE sequence on a 7T MR whole body system (Magnetom, Siemens Healthcare, Erlangen, Germany) was optimized for in vivo imaging of the human infantile knee using a 28-channel knee coil (QED, Quality Electrodynamics, Mayfield Village, OH, USA). The methods for combining and unwrapping multiple coil data described in sections 4.1 and 4.2 were all executed using MATLAB and assembled in a reconstruction pipeline shown in Fig.15. The quality of the coil combination was assessed for each of the approaches using the Q-ratio concept which is introduced in section (5.4.1). SWI results were generated according to the common procedure, that is multiplying a mask derived from the combined phase information by the magnitude image a number of times (Fig.11). Contrast to noise (CNR) in the

SWI results from each of the coil combination methods was calculated as a function of mask applications in order to obtain the optimum number of mask multiplications. The SWI results with the highest CNR were then compared visually among the different approaches for the ability to visualize veins and growing zones in the cartilage, to determine the optimum coil combination strategy for SWI of knee cartilage. A QSM was calculated from data combined with the COMPOSER and the Adaptive Combine approaches, and utilized for tSWI, in order to demonstrate differences between the SWI and tSWI results and the potential advantage of utilizing susceptibility rather than phase information for knee imaging.

Data was acquired from six healthy children of age 6, 10, 10, 11, 13 and 15 years. The 15-year old subject was female, all other subjects were male. The study was approved by the ethics committee of the Medical University of Vienna.

5.1 MR Measurements

5.1.1 T_2^* - Mapping

T_2^* -mapping of cartilage serves as a biomarker and provides insight into the composition of the collagen network. Additionally, the T_2^* -relaxation times of a tissue is a determining factor for the choice of the echo time in GE sequences. For this reason, three T_2^* -maps of knee cartilage from one adult (25 year old) and two children of age 15 and 6 years were calculated from a voxel wise exponential fit of the form $A_0 e^{(-\frac{t}{T_2^*})}$ to data from a multi-echo 3D GE scan (see Table.1). For the adult patient, a sequence of higher resolution was used in order to obtain sufficient signal from the much thinner cartilage in the adult knee. The T_2^* - fitting algorithm was preexisting and executed in MATLAB.

<i>Patient</i>	<i>25-year old</i>	<i>15-year old</i>	<i>6-year old</i>
Sequence Type	3D GE	3D GE	3D GE
Acquisition Matrix	648x768x33	132x192x32	132x192x32
Voxel dimension [mm]	0.2x0.2x2.4	0.8x0.8x3.1	0.8x0.8x3.1
Number of Echos	5	10	7
Acquisition time [s]	60	178	61

Table 1: Sequence parameters for the three T_2^* acquisitions.

5.1.2 SWI - Sequence

To optimize a GE sequence for the purpose of SWI, imaging parameters were set according to the findings of Deistung et al. [32]. Because the patients scanned were children of age 6-15 years, utmost concern was given to abide by the limits of RF power deposition - denoted as specific absorption rate (SAR) - and to assure the minimum acquisition time possible.

For the voxel geometry an aspect ratio (AR) of 4 was used, i.e. slice thickness was chosen to be four times the in plane voxel dimension. Because it was assumed that the observation concerning the optimum echo time for SWI of the brain from Ref. [32], can be well adopted for imaging the knee cartilage, $T_E = 14\text{ ms}$ was taken as a starting value. Given the need for minimizing the acquisition time T_A , echo time was gradually reduced and found to be sufficiently long at $T_E = 10\text{ ms}$ to yield visible contrast for venous vessels in the magnitude image. Table 2 shows a summary of the imaging parameters for the SWI sequence.

<i>Sequence Type</i>	<i>3D Gradient Echo</i>
Acquisition Matrix	308x448x88
Voxel Dimension [mm]	0.31x0.31x1.24
Voxel Aspect Ratio	4
Number of Echos	1
Echo Time [ms]	10.3
Flip Angle [degrees]	9
Acquisition Time [s]	189
GRAPPA Factor	3

Table 2: Imaging parameters for the SWI GE-sequence.

5.1.3 Variable Echo Time Sequence

The COMPOSER reconstruction of multiple coil data necessitates an additional reference scan of variable echo time (vTE). Only for a low resolution reference scan, data can be acquired during an ultra short T_E . Tab.3 shows the details for the vTE reference scan used.

<i>Sequence Type</i>	<i>3D Gradient Echo</i>
Acquisition Matrix	128x64x40
Voxel Dimension [mm]	1.8x1.8x2.3
Number of Echos	1
Variable Echo Time [ms]	0.8
Flip Angle [degrees]	4
Acquisition Time [s]	35
GRAPPA Factor	2

Table 3: Sequence parameters for the vTE-reference scan.

5.2 Reconstruction Pipeline

The approaches to combine and unwrap phase images introduced in section 4 were implemented in a reconstruction pipeline shown in Fig.15. The pipeline consists of two main strategies. Strategy 1 unwraps and removes offsets from the phase images individually, and then combines these by the weighted mean approach. Strategy 1 consists of two different approaches. The first uses Homodyne Filtering (1a) of complex coil data to unwrap and remove phase offsets. The second uses the Fourier-based approach (1b) to unwrap phase images prior to high-pass filtering these in order to remove the slowly varying receiver phase offsets. The spatial algorithms PRELUDE and PHUN are set in brackets since they fail in unwrapping phase information from the difficult geometry in the knee due to disconnected and highly wrapped regions.

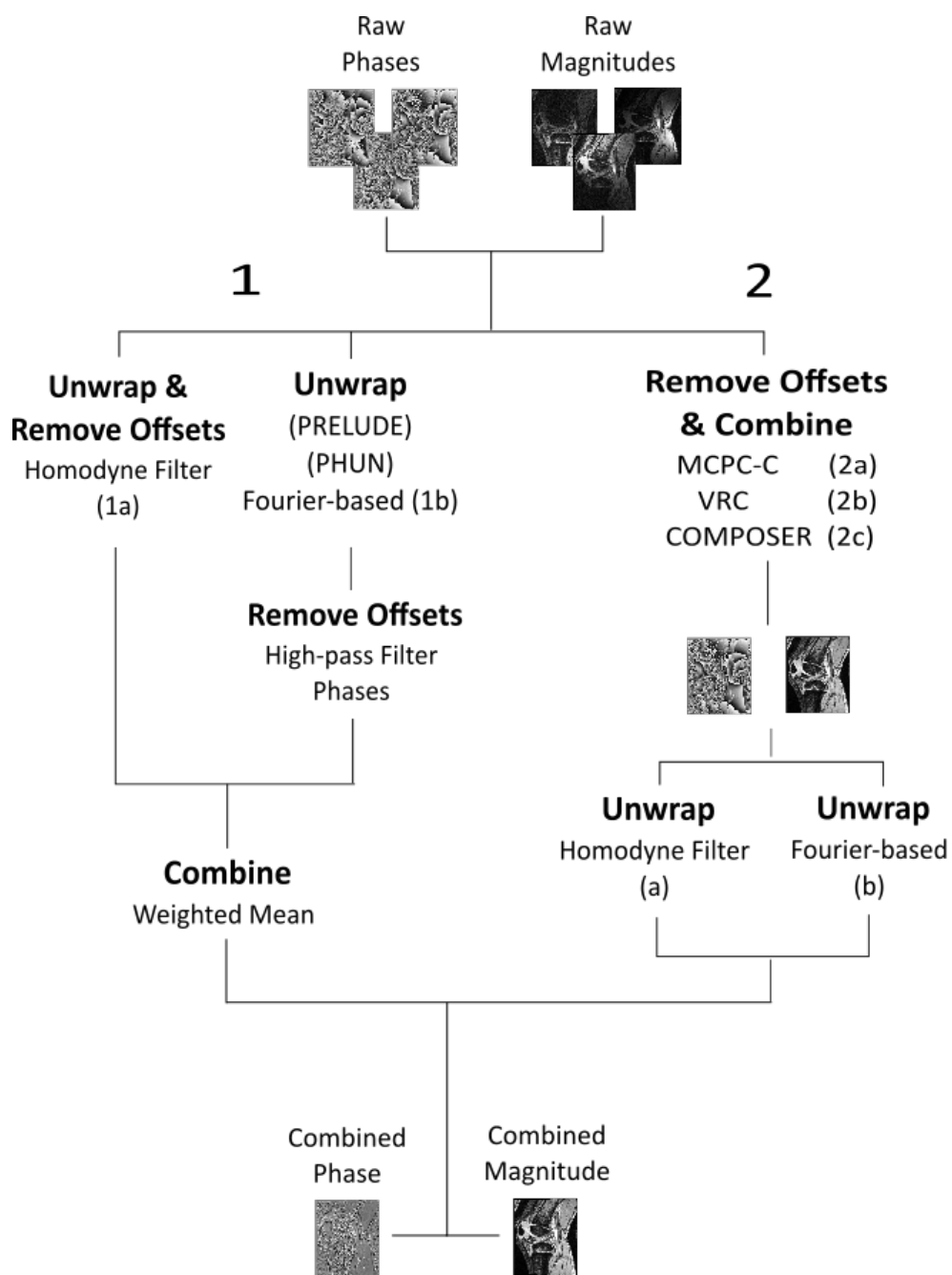


Figure 15: The reconstruction scheme for multiple coil data consists of two main strategies. 1) Unwrap & Offset Removal of individual phase images prior to combination. 2) Removing phase offsets from all coils and combining data, prior to unwrapping the combined phase image.

Strategy 2 removes phase offsets and then combines multiple coil data first, before unwrapping the combined phase image. For coil combination the MCPC-C (2a), the VRC (2b) and the COMPOSER (2c) approaches were implemented, and for unwrapping the combined phase images generated from these either Homodyne Filtering (a) or Fourier-based unwrapping (b) was employed.

In the course of this work the Homodyne Filter (1a) and the MCPC-C (2a) approach as well as the reconstruction pipeline were implemented. PRELUDE, PHUN, the

Fourier-based unwrapping algorithm as well as the VRC (2b) and the COMPOSER (2c) coil combination approaches had been established previously and were adopted for images of the knee. The approaches shown in Fig.15 were tested on data acquired from the 6-year old subject.

5.2.1 Strategy 1: Single Coil Unwrapping and Weighted Mean Combination

The critical step in combining multiple coil data using single-coil unwrapping, is the amount of high-pass filtering employed. In order to determine the minimum amount of high-pass filtering needed for both approaches in strategy 1 to achieve high-quality phase matching, data was combined once for omitting high-pass filtering at all, and for varying filter widths of $\sigma = [80 \times 80, 20 \times 20, 5 \times 5, 2 \times 2]$ for a 2D Gaussian filter and compared between both approaches. Whereas Homodyne Filtering was achieved by dividing complex data by a Gaussian low-pass filtered version of it (as described in section 4.1.1), high-pass filtering in the second approach in strategy 1 (1b) was achieved by subtracting Gaussian low-pass filtered versions from the original phase images according to:

$$\phi_{uw,l}^{HP} = \phi_{uw,l} - \phi_{uw,l}^{LP} \quad (5.1)$$

where $\phi_{uw,l}$ is the unwrapped phase of coil l , $\phi_{uw,l}^{LP}$ is the low-pass filtered version and $\phi_{uw,l}^{HP}$ is the resulting high-pass filtered unwrapped phase.

5.2.2 Strategy 2: Phase Matching by Removing Phase Offsets

Smoothing of the reference phase offsets (RPOs) in the VRC approach (2b) was achieved using a 2D Gaussian low-pass filter for widths of $\sigma = [15 \times 15, 10 \times 10, 5 \times 5, 3 \times 3]$ to obtain the optimum amount of low-pass filtering. For the Homodyne Filter

implemented in Strategy 2, a 2D Gaussian low-pass filter of width $\sigma = 3 \times 3$ was used to achieve sufficient removal of wraps in the combined phase images generated by the three different coil combination approaches.

5.3 SWI - Processing

For generating SWI results from the combined phase and magnitude images obtained with the approaches shown Fig.(15), the procedure shown in Fig.(11) was carried out. Phase images were high-pass filtered according to Eq.(5.1) in the previous section, with a 3×3 Gaussian filter kernel. The filtered phase then was converted into a positive phase mask by rescaling phase values according to Fig.(10). SWI results were obtained by multiplying this phase mask into the magnitude image for a typical number of $n=[1-8]$ times (as commonly reported in literature), to find the multiplication factor which yields optimum CNR.

5.4 Analysis

5.4.1 Phase Matching

The quality of matching individual phase information from the multitude of coils was evaluated by calculating the ratio between the sum over individual coil magnitudes and the magnitude of the sum of phase-corrected complex coil signals according to Ref.[33]:

$$Q = 100 \times \frac{|\sum_l M_l e^{i\phi_l}|}{\sum_l M_l} \quad (5.2)$$

where the index l denotes coils and Q reflects the degree of phase congruence among the multiple coil signals.

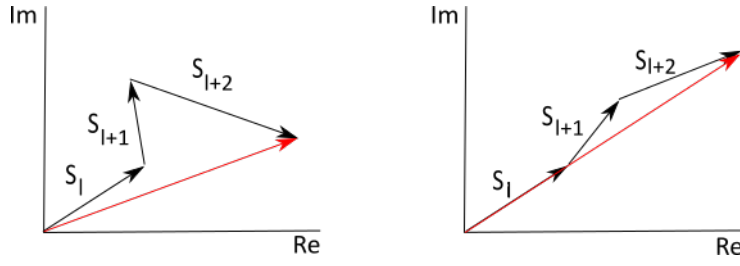


Figure 16: Two examples of phase matching among signals S from three coils l , $l+1$ and $l+2$. Phase matching shown in the left image is bad (low Q-ratio), phase matching shown in the right image is good (high Q-ratio).

5.4.2 SWI Results

In order to obtain the optimum number of mask application for the SWI result from the combined images obtained with each of the approaches in Fig.(15), CNR in the SWI results was calculated for a range of [1-8] mask multiplications. CNR was calculated as the signal difference between a ROI in a homogeneous region of the cartilage and a ROI covering a vein, divided by the standard deviation in the cartilage ROI.

$$CNR = \frac{\bar{S}_{ROI, cartilage} - \bar{S}_{ROI, vein}}{\sigma_{cartilage}} \quad (5.3)$$

where the bar over S denotes the mean signal in the ROI. For each approach, the optimum number of mask multiplication was obtained from the SWI showing the highest CNR. In order to compare the quality of the different approaches for SWI, CNR and the visibility of venous structures and zones in the cartilage were observed.

In order to avoid bias between the CNR calculation and the SWI result from any of the implemented approaches, the ROIs were created within an image derived from averaging over all five SWI results.

5.5 QSM - Algorithm

A very recent algorithm from Langkammer et al. [11] was used to calculate QSM images for data from both the 6-year old and the 13-year old subject. The algorithm takes magnitude and phase information as an input. Additionally, a mask was introduced to the calculation to suppress noisy regions outside the knee and signal of low SNR within the bones, which was created by thresholding the magnitude image. The ratio for the TV-regularization parameters was taken as $\frac{\alpha_0}{\alpha_1} = 2$, as recommended in Ref.[11]. The number of iterations was set to 2000, and the algorithm was executed from a PYTHON script.

The QSM image for the 6-year old subject was calculated for data combined with the COMPOSER approach, and two QSM images for the 13-year old subject were obtained from data combined with both the COMPOSER and the Adaptive Combine approach, to demonstrate anticipated artefacts when the latter approach is used.

5.6 True SWI - Processing

True SWI (tSWI) images were calculated from the QSM images obtained from the 6-year old and the 13-year old subject. For the tSWI processing of both QSM images, high-pass filtering was performed according to Eq.(5.1) using a 4x4 2D Gaussian filter and a positive susceptibility mask was multiplied 4-times by the magnitude image. The contrast in the tSWI image for the 6-year old subject was enhanced by generating a mIP over 4 slices.

6 Results

6.1 T_2^* -Maps of Knee Cartilage

Fig.17 shows the T_2^* - maps of knee cartilage from a 6-year-old (a), a 15-year-old (b) and a 25-year-old (c) subject overlaid in a colored scale on the respective GE magnitude images. The similarity in the range of T_2^* - values between Fig.17(b) and Fig.17(c) is striking, indicating that the development of knee cartilage at an age of 15 is more or less complete. The T_2^* distribution in Fig.17(b) shows higher values in the range of 20 - 40 ms along a line, probably representing a distinct zone in the cartilage characterized by specific alignment of collagen fibers. In contrast to the older subjects, the T_2^* - map of the 6-year-old (Fig.17(a)) shows a highly inhomogeneous distribution of values, which arises from an inhomogeneous composition of the cartilage due to blood vessels and different zonal growing regions in very young cartilage. Regions of high values in Fig.17(a) range from 30-70 ms. The red arrow in Fig.17(a) points to a number of voxels for which the fit generated unreliably high values, probably due to a very fast signal decay caused by venous blood. These voxels were set to the maximum of the scale shown in Fig.17.

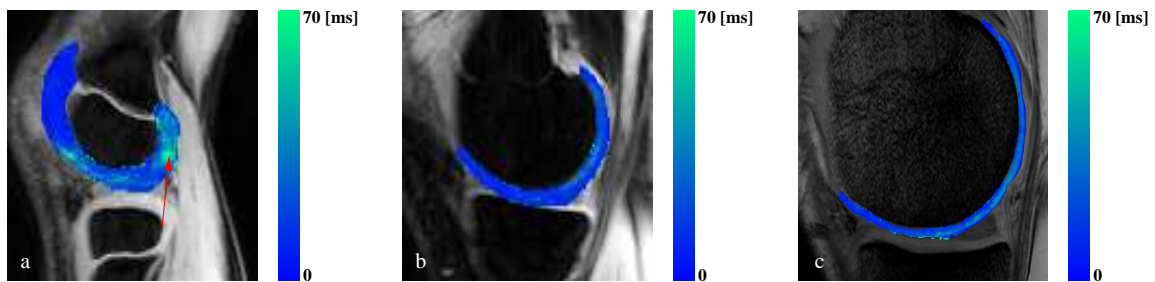


Figure 17: T_2^* - maps of knee cartilage for a 6-year old (a), a 15-year old (b) and a 25-year old (c) subject.

6.2 Combination of Multiple Coil Data

Fig.18 shows the SOS reconstructed magnitude (left) and the combined phase image (right) from the scanner. The red box encompasses the thick knee cartilage typical in young children. The phase image shown in Fig.18 demonstrates the severe problem of wraps due to the complicated magnetic environment in the knee.

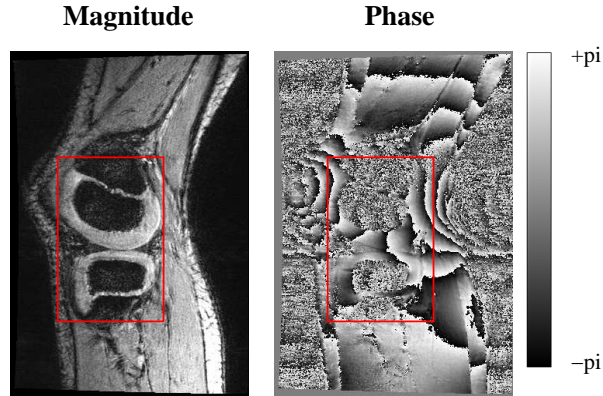


Figure 18: Magnitude and phase image reconstructed with the SOS-approach from the scanner. The red box contains the knee cartilage, to which SWI is restricted to in this work.

6.2.1 Single Coil Unwrapping and Weighted Mean Combination (Strategies 1a and 1b)

In order to compare the quality of the two reconstruction approaches from strategy 1 in Fig.15, i.e. 1a and 1b, Fig.19 shows pairs of the combined phase images and the corresponding Q-ratios for particular high-pass filter sizes. The top row in Fig.19 shows the results when phase images are not filtered at all, which in case of the Homodyne Filter approach this means that the measured wrapped phase images are directly combined by the weighted mean approach, which results in bad phase matching and a combined phase containing numerous wraps. In contrast to that, Fourier-based unwrapping of phase images without subsequent high-pass filtering is already sufficient to obtain phase matching of around 80%. For decreasing filter size, i.e. increasing high-pass filtering, Fig.19 shows that phase wraps are progressively

removed by Homodyne Filtering, which results in better phase matching reflected in the Q-ratios. However, perfect phase matching in the Homodyne Filter approach is reached only for extreme high-pass filtering, whereas Fourier-based single-coil unwrapping yields perfect phase matching for much weaker high-pass filtering. For the fact that high-pass filtering of phase images is critical, Fourier-based single-coil unwrapping is clearly superior to Homodyne Filtering. As a result of this, the Homodyne Filter approach was excluded from further considerations to generate SWI images from.

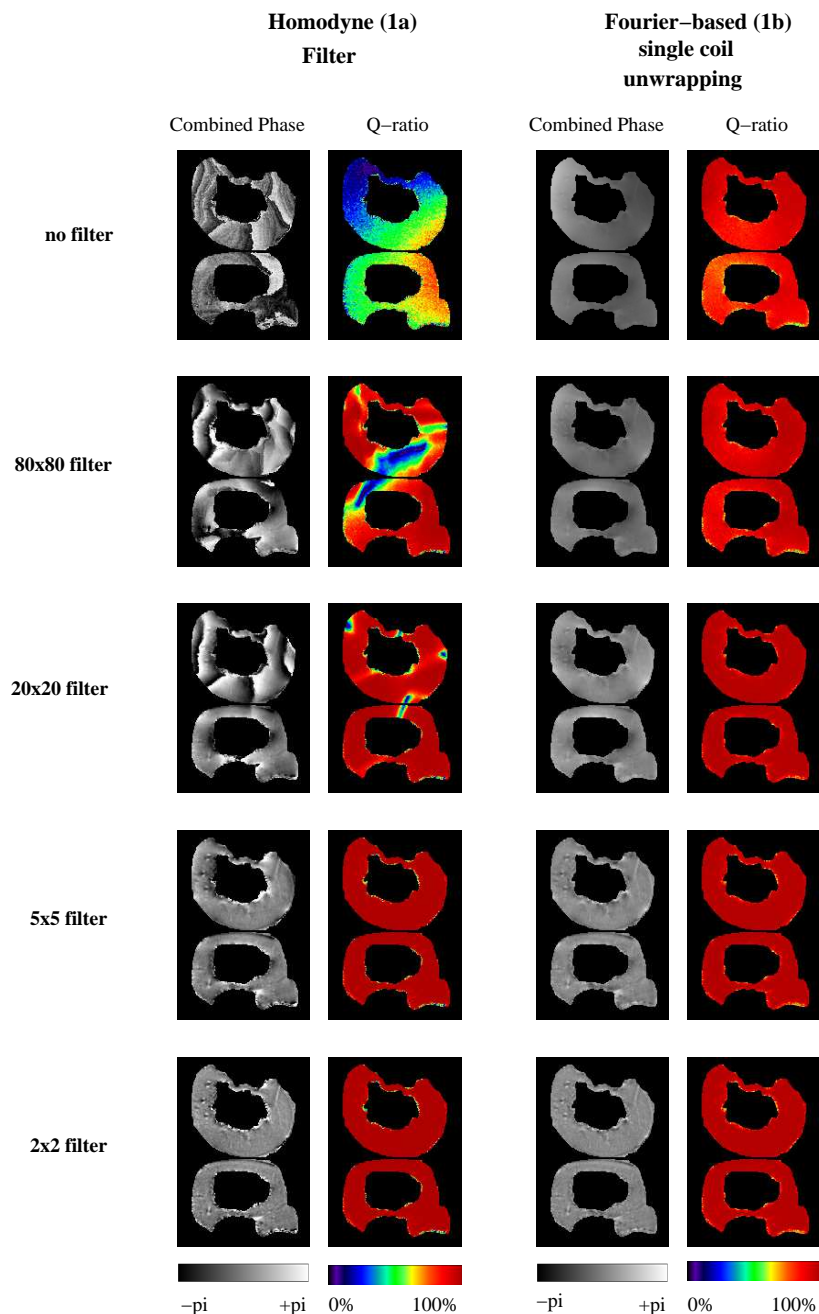


Figure 19: Comparison of the two approaches from strategy 1 in Fig.(15), i.e. the Homodyne Filter (1a) and the Fourier-based single coil unwrapping (1b). Shown are pairs of the combined phase image and the corresponding Q-ratio for a particular high-pass filter size.

6.2.2 Phase Matching by Removing Phase Offsets (Strategies 2a, 2b and 2c)

Coil combination with the MCPC-C (2a) and the COMPOSER (2c) approach is straightforward. For combining coils using the VRC (2b) approach, the effect of

low-pass filtering the reference phase offsets (RPOs) has to be investigated, in order to assure high-quality phase matching.

The quality of combining phase images using the Virtual Reference Coil approach highly depends on the degree of smoothing of the RPOs. Fig.20 shows Q-ratios for VRC-combined data obtained with different sizes of low-pass filters in image space. When the filter size is too large, smoothing of the RPOs leads to loss of information, which results in inaccurate matching of phase information from individual coils to the Virtual Reference Coil phase (Fig.20(a)). Better phase matching is achieved using smaller filter sizes as shown in Fig.20(b) and Fig.20(c). Perfect phase matching is achieved using a 3x3 Gaussian filter for smoothing the RPOs (Fig.20(d)). The results shown in Fig.20 demonstrate the importance of choosing a small filter kernel for smoothing, since larger filter kernels cause attenuation of important spatial variations in the RPO - maps.

Virtual Reference Coil Combination (2b) – Q-ratio for different smoothing of RPOs

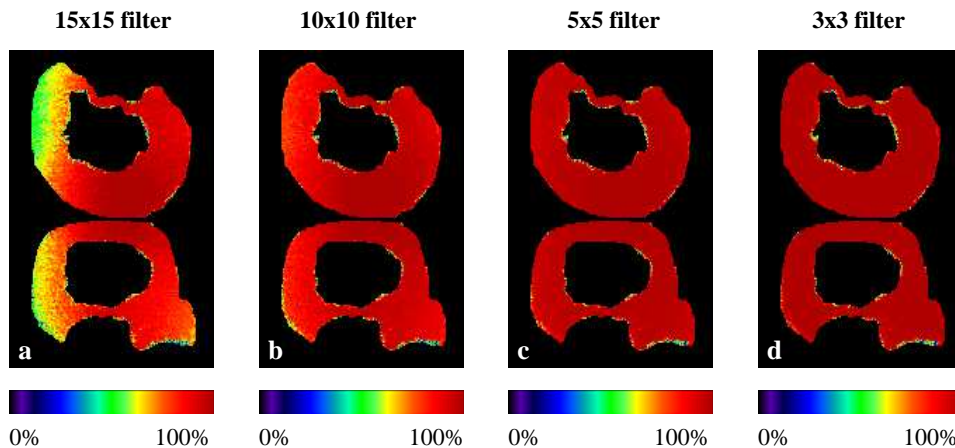


Figure 20: Q-ratios for the VRC - approach for different smoothing of the reference phase offsets (RPOs). The filter size strongly affects the quality of phase matching.

Fig.21 shows a comparison of the phase matching performed by the three approaches from strategy 2. For the VRC approach the optimum result from Fig.20 is shown, i.e. the result generated using a 3x3 low-pass filter. The MCPC-C approach shows near perfect phase matching within knee cartilage (Fig.21(a)), but worse phase matching in outer regions of the knee (Fig.21(d)), i.e. in regions distant to the central point

of matching the coil phase images. In contrast to that, quality of phase matching is perfect within knee cartilage and throughout the entire FOV for both the VRC and the COMPOSER approach. Given this, the MCPC-C approach was not considered for generating SWI of the knee cartilage.

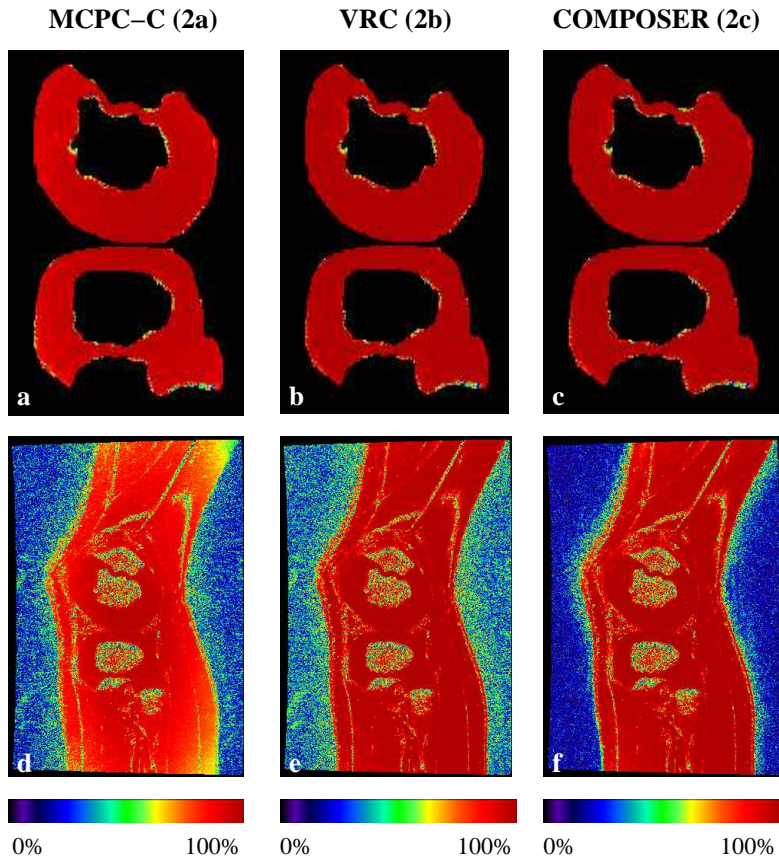


Figure 21: Comparison of the three approaches from strategy 2 in Fig.(15). Quality of phase matching is shown for the knee cartilage (a-c) and for the whole FOV (d-f).

6.3 Susceptibility Weighted Images

The combined and high-pass filtered phases from all implemented methods including the scanner-implemented homodyne filter method are shown in Fig.23 (a-f). All approaches remove phase wraps and show contrast for veins viewed in both the in plane direction (blue arrow) and the through plane direction (red arrows). To some extent, phase images also show contrast for a border between different zones in the

lower cartilage (green arrow).

For each approach implemented, SWI images were generated for a range of [1-8] mask multiplications and for each of these images, CNR was calculated according to Eq.(5.3). The SWI software on the scanner delivers only a single SWI image, which is generated by a 4-times mask multiplication.

CNR as a function of the number of mask multiplications for each of the implemented approaches is shown in Fig.22. It can be observed that the characteristics of the CNR-curves is determined by the method used for unwrapping, i.e either Fourier-based unwrapping or Homodyne Filtering.

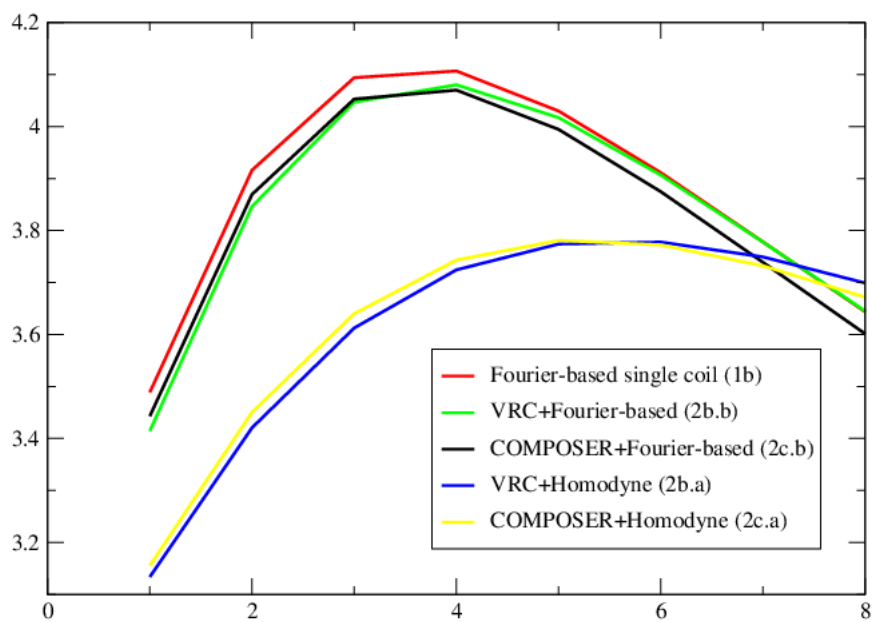


Figure 22: CNR vs number of mask multiplications for SWI results of implemented methods.

All approaches which use Fourier-based unwrapping show higher CNR than the approaches using Homodyne Filtering to unwrap. Also, the approaches using Fourier-based unwrapping reach the optimum CNR for a 4-times mask application, whereas the VRC+ and the COMPOSER+Homodyne Filter approach need more multipli-

cations to reach optimum CNR , i.e. a 6-times and a 5-times mask multiplication respectively.

<i>Approach</i>	<i>n</i>	<i>CNR(n)</i>
Scanner-implemented Homodyne Filter	4	3.75
Fourier-based single coil unwrapping (1b)	4	4.11
VRC + Homodyne unwrapping (2b.a)	6	3.78
VRC + Fourier-based unwrapping (2b.b)	4	4.08
COMPOSER + Homodyne unwrapping (2c.a)	5	3.78
COMPOSER + Fourier-based unwrapping (2c.b)	4	4.07

Table 4: Details for the SWI results shown in Fig.23.

Fig.23(g-l) shows the SWI results from each approach generated with the number of mask multiplication which yields highest CNR (see Table 4). All of the approaches visualize a large vein in the in-plane direction (blue arrow) and a number of veins viewed in the through plane direction (red arrows), which appear as two black spots due to the dipolar nature of the induced field inhomogeneity. The SWI images also yield contrast for a border between different zones in the lower cartilage (green arrow), which probably arises from a change in the alignment of cartilage fibers. At a first glance, no prominent differences can be observed between the SWI images from the different approaches. However, the SWI result generated with the scanner implemented Homodyne Filter approach lacks in visualizing some of the small veins compared to the other approaches. The large vein is visualized most clearly by the Fourier-based single coil unwrapping approach, which highlights the fact that this approach achieves the highest CNR. The COMPOSER+Fourier-based unwrapping approach yields comparable visualization of the large vein.

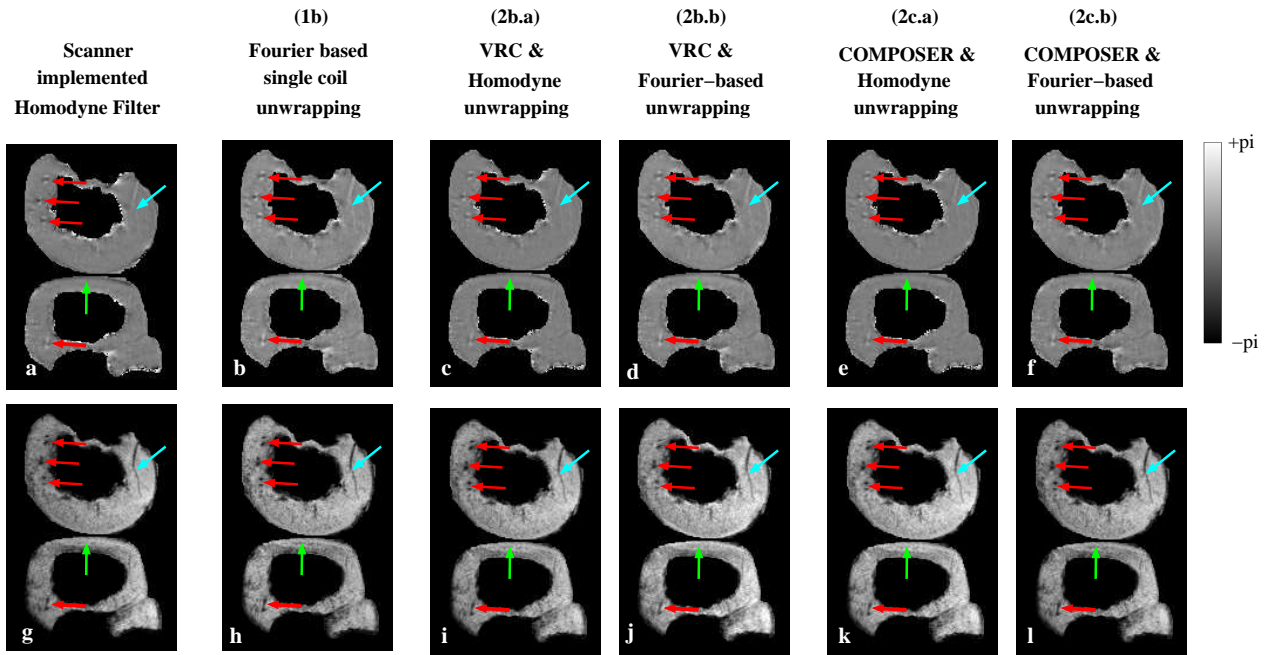


Figure 23: Comparison of the combined, high-pass filtered phase images (a-f) and the SWI results (g-l) calculated from these, for the scanner-implemented Homodyne Filter and the novel approaches implemented. Arrows point to a vein viewed in the in-plane direction (blue), to veins viewed in the through-plane direction (red) and to a border in the cartilage (green).

In order to test and verify the potential benefit of QSM of knee cartilage, artefact-free phase information of high-quality is needed. Given the simplicity and the high-quality of phase-matching, the COMPOSER approach was used to combine multiple coil phase data in order to calculate a QSM (Fig.24(b)). The QSM was used as the source of contrast information for susceptibility weighted imaging according to the common SWI processing, which has been termed true SWI (tSWI) in Ref.[31]. This tSWI image was investigated for the visualization of veins and other information complementary to magnitude, and compared to a common SWI in order to demonstrate potential benefit.

Fig.24 shows a comparison between the high-pass filtered phase (a) and susceptibility (b) information, together with the SWI and the tSWI generated from these by a 4-times mask multiplication. The red boxes indicate regions showing fundamental differences in both contrast information (phase and susceptibility) and the resulting SWI and tSWI results. It is demonstrated clearly, that the dipolar appearance of

veins in Fig.24(a) is recovered by QSM and depicted as single veins in Fig.24(b) within both red boxes. This difference in the appearance of veins is transferred to the SWI and the tSWI image. The two veins in the red boxes are depicted as two dark spots in the SWI result (Fig.24(c)), whereas in the tSWI result this doubling artefact is resolved and the veins appear as one single spot (Fig.24(d)). Additionally, tSWI resolves a vein in the in plane direction within the big red box, which is only faintly depicted in the SWI result.

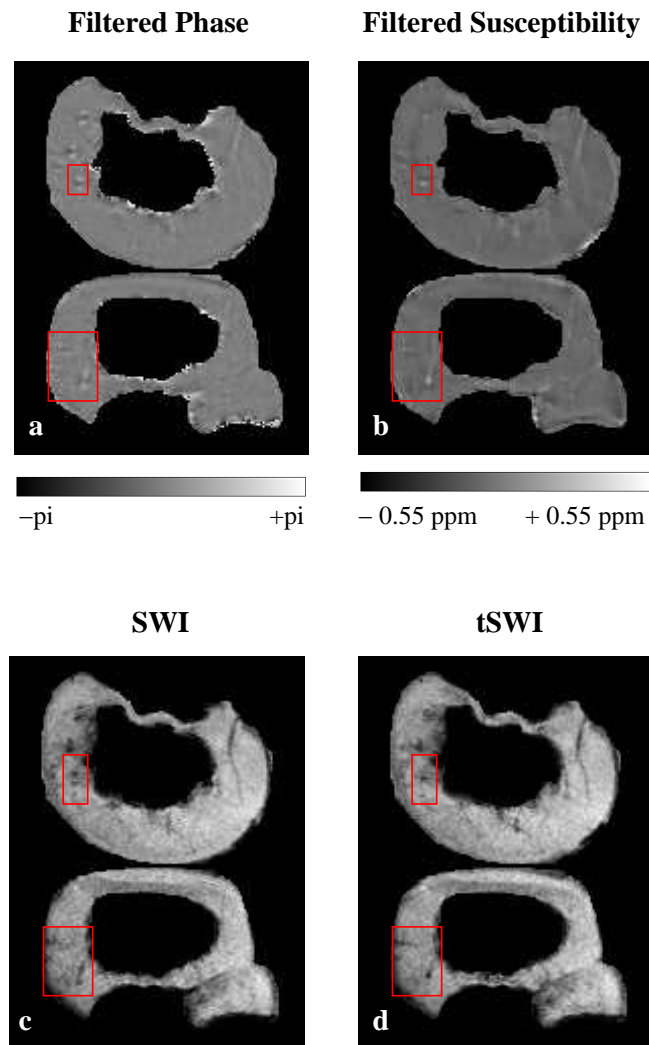


Figure 24: Comparison of a high-pass filtered phase (a) and a high-pass filtered QSM image (b) of knee cartilage. The SWI result calculated from the phase is shown in (c), and the tSWI result calculated from the QSM is shown in (d). The red boxes indicate obvious differences in both contrast information (a and b) and the susceptibility weighted images (c and d) of knee cartilage.

In a recent work, Nissi et al. [34] showed QSM and tSWI generated from phase data combined via the Adaptive Combine approach described in section 4.1.5 for imaging veins in animal cartilage. To demonstrate the limitation of this approach for the challenging case of thin knee cartilage, QSM and tSWI was calculated for data from a 13-year old male subject, and then compared to the QSM and tSWI derived from the same data combined with the COMPOSER approach. Fig.25 shows a comparison of both QSM and tSWI obtained with the COMPOSER and the Adaptive Combine approach.

The QSM calculated from phase information reconstructed with the Adaptive Combine approach shows numerous artefacts (red arrows in Fig.25(a)) which originate from areas of incorrect coil combination. These artefacts emulate areas of high susceptibility, which yield wrong contrast in the tSWI result (red arrows in Fig.25(c)). In contrast to the Adaptive Combine approach, both the QSM and the tSWI result obtained from phase data combined with the COMPOSER approach show no artefacts (Fig.25(b) and (d)).

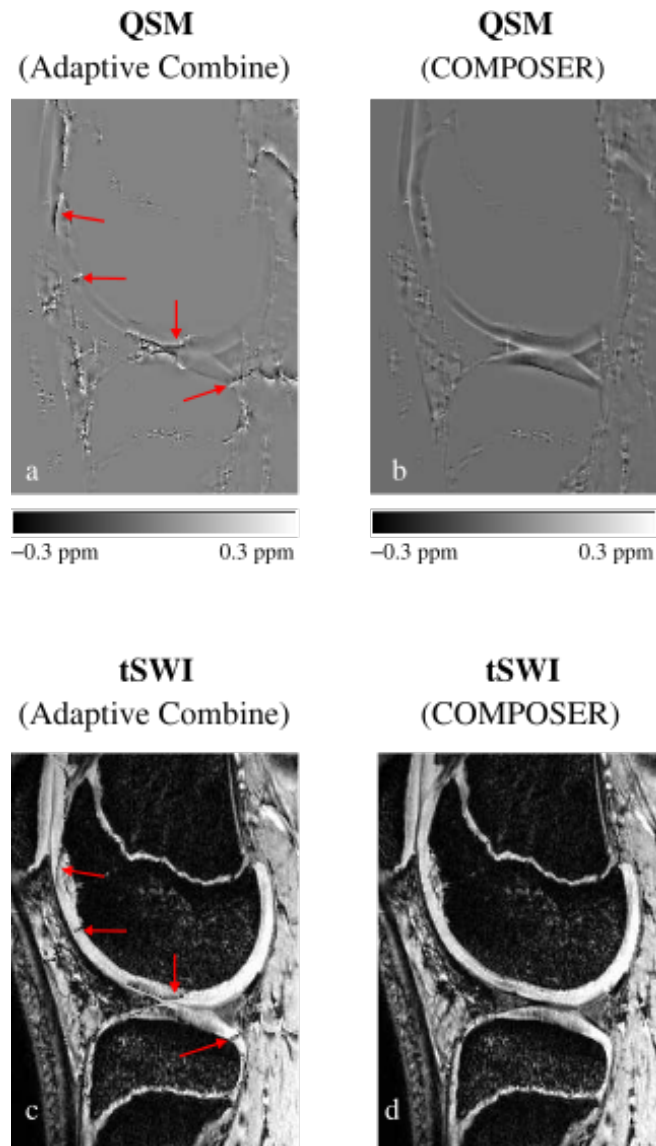


Figure 25: Comparison of the QSM obtained from the Adaptive Combine approach (a) as in Ref.[34] and the COMPOSER approach (b). The tSWI results generated from these are shown in (c) and (d). Red arrows in (a) point to artefacts originating from incorrect coil combination, which degrade the tSWI-result (c).

In order to demonstrate the power of the implemented tSWI approach to generate complementary contrast information to the magnitude image, Fig.26 shows a comparison between the minimum intensity projection (mIP) of the magnitude image (left column) and the mIP of the tSWI image (right column) for three slices of an infantile knee. Venous structures are strongly enhanced in the mIP tSWI in Fig.26(b) and (f). Comparison of Fig.26(c) and (d) shows that tSWI yields also contrast for the boarder zone between articular cartilage and the cartilage enclosing the patella.

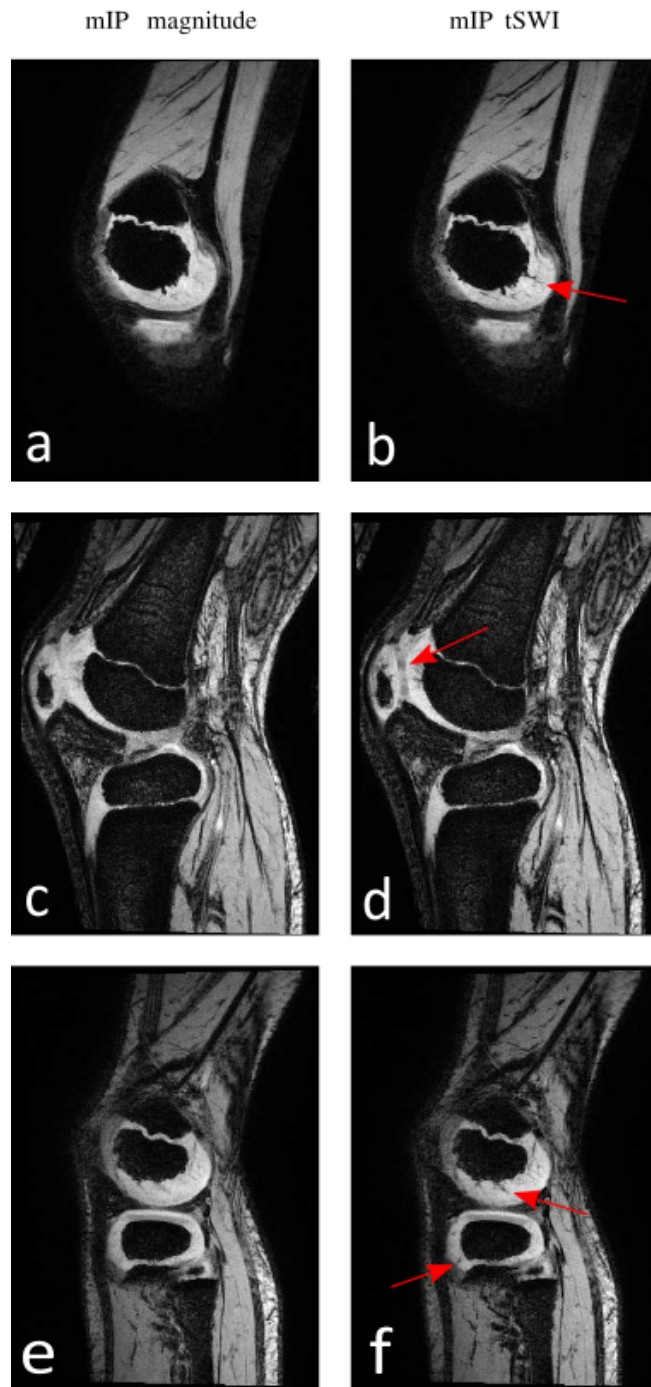


Figure 26: Demonstrating the effect of tSWI of the knee. The left column shows mIPs of magnitude images and the right column shows mIPs of tSWI results for three different slices of an infantile knee. The mIP tSWI images show contrast enhancement of venous structures in (b) and (f), and novel contrast for the border between articular and patella cartilage (red arrow in d).

7 Discussion

A GE sequence for SWI of the infantile knee was optimised, and numerous approaches to combine multiple coil signals from a phased array and the feasibility of these for SWI were assessed. Additionally, QSM and tSWI of knee cartilage was performed, which drastically improved visualization of veins due to resolving the doubling artefact seen in conventional SWI using phase information. Imaging very young subjects necessitated minimum acquisition time, i.e. a high acceleration factor for data acquisition was used. For this reason, SNR in the SWI results is low compared to in vivo and ex vivo animal studies in Ref.[35, 34].

The simplistic Homodyne Filter approach to unwrap and combine phase images, which is still widely used, was shown to be unfeasible for the use of SWI of the knee due to the excessive high-pass filtering needed. For the first time, Fourier-based unwrapping was implemented to unwrap phase images from multiple coils separately, which allows for much less high-pass filtering compared to the Homodyne Filter approach. However, Fourier-based unwrapping generates artificial regions of high phase values at the border of the image. These have to be set to zero prior to the creation of the phase mask, because otherwise the effect for the phase values of interest is attenuated. The recently established methods for phase matching of multiple coil data - the VRC and the COMPOSER approach - have been tested successfully for knee imaging for the first time. Beside the fact that an additional reference scan is needed, the COMPOSER approach is a more simple and practical method than the VRC approach, which relies on low-pass filtering and fails when phase matching for generating the virtual reference coil fails.

Unwrapping phase information reconstructed with either the VRC or the COMPOSER approach was achieved in two ways - by Homodyne Filtering and Fourier-based unwrapping. Using Homodyne Filtering for unwrapping represents an additional high-pass filtering step in the process towards the SWI result, compared to unwrapping with the Fourier-based approach. Therefore, the amount of noise

in the combined and high-pass filtered phase information obtained with both the VRC+Homodyne and the COMPOSER+Homodyne approaches is higher compared to both the VRC+Fourier-based unwrapping and the COMPOSER+Fourier-based unwrapping approaches. The increased amount of noise in the phase information is transferred into the SWI result by the application of the phase mask, which leads to the reduced CNR seen in Fig.22. For a fair comparison of the two unwrapping strategies concerning the quality of the SWI result, the high-pass filtering step in the SWI-processing scheme in Fig.11 should be omitted for the case of unwrapping using the Homodyne Filter.

Phase information reconstructed with the COMPOSER approach was used for QSM of knee cartilage, due to easy practicability and excellent quality of phase matching. However, when there is no reference scan available for the SWI data, phase information reconstructed with the VRC approach could serve as equivalently reliable input for the calculation of a QSM. The QSM of knee cartilage from a six-year old subjects was employed for tSWI, which showed improved visualization of veins due to the resolution of the doubling artefact seen in conventional SWI. Additionally, it was shown in Fig.25 that using phase information reconstructed with the Adaptive Combine approach for QSM of thin knee cartilage results in artefacts, degrading the tSWI result. In contrast to that, the COMPOSER approach provides phase information from which a reliable QSM is derived, yielding an artefact-free tSWI result.

Imaging the entire venous vasculature including even very small veins remains to be achieved, which would necessitate refinement of data acquisition by measures to increase resolution and SNR. Additionally, moderate prolongation of data acquisition time, i.e. using a lower acceleration factor for the measurement, would increase SNR in the magnitude image. These measures would probably help to image more subtle parts of the vasculature within growing knee cartilage, which would allow for studying the relationship between vessel disturbances and ossification disorders in young patients.

8 Conclusion

This work demonstrated the first human in vivo SWI of infantile knee cartilage at 7T. Visualization of large veins as well as increased contrast for zones within the articular cartilage has been shown. Three possible processing pipelines have been established for SWI of the knee which are improvements on the methods used in phase contrast imaging to date. This work is being applied in an ongoing study of cartilage channels and cartilage zones in osteochondritis dissecans at 7T in juvenile patients.

References

- [1] E. M. Haacke, Y. Xu, Y.-C. N. Cheng, and J. R. Reichenbach, “Susceptibility weighted imaging (SWI),” *Magnetic Resonance in Medicine*, vol. 52, no. 3, pp. 612–618, 2004.
- [2] C. Carlson, H. Hilley, and D. Meuten, “Degeneration of cartilage canal vessels associated with lesions of osteochondrosis in swine,” *Veterinary Pathology Online*, vol. 26, no. 1, pp. 47–54, 1989.
- [3] B. Ytrehus, C. Carlson, and S. Ekman, “Etiology and pathogenesis of osteochondrosis,” *Veterinary Pathology Online*, vol. 44, no. 4, pp. 429–448, 2007.
- [4] E. M. Haacke and J. R. Reichenbach, *Susceptibility weighted imaging in MRI: basic concepts and clinical applications*. John Wiley & Sons, 2014.
- [5] K. P. Pruessmann, M. Weiger, M. B. Scheidegger, P. Boesiger *et al.*, “SENSE: sensitivity encoding for fast MRI,” *Magnetic resonance in medicine*, vol. 42, no. 5, pp. 952–962, 1999.
- [6] M. A. Griswold, P. M. Jakob, R. M. Heidemann, M. Nittka, V. Jellus, J. Wang, B. Kiefer, and A. Haase, “Generalized autocalibrating partially parallel acquisitions (GRAPPA),” *Magnetic resonance in medicine*, vol. 47, no. 6, pp. 1202–1210, 2002.
- [7] P. B. Roemer, W. A. Edelstein, C. E. Hayes, S. P. Souza, and O. Mueller, “The NMR phased array,” *Magnetic resonance in medicine*, vol. 16, no. 2, pp. 192–225, 1990.
- [8] K. Shmueli, J. A. de Zwart, P. van Gelderen, T.-Q. Li, S. J. Dodd, and J. H. Duyn, “Magnetic susceptibility mapping of brain tissue in vivo using MRI phase data,” *Magnetic Resonance in Medicine*, vol. 62, no. 6, pp. 1510–1522, 2009.

- [9] J. Marques and R. Bowtell, "Application of a Fourier-based method for rapid calculation of field inhomogeneity due to spatial variation of magnetic susceptibility," *Concepts in Magnetic Resonance Part B: Magnetic Resonance Engineering*, vol. 25, no. 1, pp. 65–78, 2005.
- [10] E. Haacke, J. Tang, J. Neelavalli, and Y. Cheng, "Susceptibility mapping as a means to visualize veins and quantify oxygen saturation," *Journal of Magnetic Resonance Imaging*, vol. 32, no. 3, pp. 663–676, 2010.
- [11] C. Langkammer, K. Bredies, B. A. Poser, M. Barth, G. Reishofer, A. P. Fan, B. Bilgic, F. Fazekas, C. Mainero, and S. Ropele, "Fast quantitative susceptibility mapping using 3D EPI and total generalized variation," *NeuroImage*, vol. 111, pp. 622–630, 2015.
- [12] D. C. Noll, D. G. Nishimura, and A. Macovski, "Homodyne detection in magnetic resonance imaging," *Medical Imaging, IEEE Transactions on*, vol. 10, no. 2, pp. 154–163, 1991.
- [13] K. E. Hammond, J. M. Lupo, D. Xu, M. Metcalf, D. A. Kelley, D. Pelletier, S. M. Chang, P. Mukherjee, D. B. Vigneron, and S. J. Nelson, "Development of a robust method for generating 7.0 T multichannel phase images of the brain with application to normal volunteers and patients with neurological diseases," *Neuroimage*, vol. 39, no. 4, pp. 1682–1692, 2008.
- [14] A. Rauscher, M. Barth, J. R. Reichenbach, R. Stollberger, and E. Moser, "Automated unwrapping of mr phase images applied to BOLD MR-venography at 3 Tesla," *Journal of Magnetic Resonance Imaging*, vol. 18, no. 2, pp. 175–180, 2003.
- [15] P. Jezzard and R. S. Balaban, "Correction for geometric distortion in echo planar images from B0 field variations," *Magnetic resonance in medicine*, vol. 34, no. 1, pp. 65–73, 1995.

- [16] S. Robinson and J. Jovicich, “B0 mapping with multi-channel RF coils at high field,” *Magnetic Resonance in Medicine*, vol. 66, no. 4, pp. 976–988, 2011.
- [17] M. A. Bernstein, M. Grgic, T. J. Brosnan, and N. J. Pelc, “Reconstructions of phase contrast, phased array multicoil data,” *Magnetic resonance in medicine*, vol. 32, no. 3, pp. 330–334, 1994.
- [18] D. L. Parker, A. Payne, N. Todd, and J. R. Hadley, “Phase reconstruction from multiple coil data using a virtual reference coil,” *Magnetic Resonance in Medicine*, vol. 72, no. 2, pp. 563–569, 2014.
- [19] B. W. D. B. C. P. G. G. D. X. B. O. Robinson, S. and S. Trattnig, “Combining phased array data using offsets from a short echo-time reference scan (COMPOSER),” *Proc. Intl. Soc. Mag. Reson. Med.* 23, 3308, 2015.
- [20] X. Deligianni, P. Bär, K. Scheffler, S. Trattnig, and O. Bieri, “High-resolution fourier-encoded sub-millisecond echo time musculoskeletal imaging at 3 Tesla and 7 Tesla,” *Magnetic Resonance in Medicine*, vol. 70, no. 5, pp. 1434–1439, 2013.
- [21] D. O. Walsh, A. F. Gmitro, and M. W. Marcellin, “Adaptive reconstruction of phased array MR imagery,” *Magnetic Resonance in Medicine*, vol. 43, no. 5, pp. 682–690, 2000.
- [22] S. M. Verbout, C. M. Netishen, and L. M. Novak, “Polarimetric techniques for enhancing SAR imagery,” in *OE/LASE’92*. International Society for Optics and Photonics, 1992, pp. 141–173.
- [23] M. Jenkinson, “Fast, automated, N-dimensional phase-unwrapping algorithm,” *Magnetic resonance in medicine*, vol. 49, no. 1, pp. 193–197, 2003.
- [24] S. Witoszynskyj, A. Rauscher, J. R. Reichenbach, and M. Barth, “Phase unwrapping of MR images using ϕ_{un} —a fast and robust region growing algorithm,” *Medical image analysis*, vol. 13, no. 2, pp. 257–268, 2009.

- [25] R. Cusack and N. Papadakis, “New robust 3-D phase unwrapping algorithms: application to magnetic field mapping and undistorting echoplanar images,” *Neuroimage*, vol. 16, no. 3, pp. 754–764, 2002.
- [26] M. A. Schofield and Y. Zhu, “Fast phase unwrapping algorithm for interferometric applications,” *Optics letters*, vol. 28, no. 14, pp. 1194–1196, 2003.
- [27] M. Hýtch, E. Snoeck, and R. Kilaas, “Quantitative measurement of displacement and strain fields from HREM micrographs,” *Ultramicroscopy*, vol. 74, no. 3, pp. 131–146, 1998.
- [28] T. E. Gureyev and K. A. Nugent, “Phase retrieval with the transport-of-intensity equation. ii. orthogonal series solution for nonuniform illumination,” *JOSA A*, vol. 13, no. 8, pp. 1670–1682, 1996.
- [29] V. Volkov, Y. Zhu, and M. De Graef, “A new symmetrized solution for phase retrieval using the transport of intensity equation,” *Micron*, vol. 33, no. 5, pp. 411–416, 2002.
- [30] H. Bagher-Ebadian, Q. Jiang, and J. R. Ewing, “A modified fourier-based phase unwrapping algorithm with an application to MRI venography,” *Journal of Magnetic Resonance Imaging*, vol. 27, no. 3, pp. 649–652, 2008.
- [31] E. M. Haacke, S. Liu, S. Buch, W. Zheng, D. Wu, and Y. Ye, “Quantitative susceptibility mapping: current status and future directions,” *Magnetic resonance imaging*, vol. 33, no. 1, pp. 1–25, 2015.
- [32] A. Deistung, A. Rauscher, J. Sedlacik, J. Stadler, S. Witoszynskyj, and J. R. Reichenbach, “Susceptibility weighted imaging at ultra high magnetic field strengths: theoretical considerations and experimental results,” *Magnetic Resonance in Medicine*, vol. 60, no. 5, pp. 1155–1168, 2008.
- [33] S. Robinson, G. Grabner, S. Witoszynskyj, and S. Trattinig, “Combining phase images from multi-channel RF coils using 3D phase offset maps derived from a

dual-echo scan,” *Magnetic Resonance in Medicine*, vol. 65, no. 6, pp. 1638–1648, 2011.

- [34] M. J. Nissi, F. Tóth, L. Wang, C. S. Carlson, and J. M. Ellermann, “Improved visualization of cartilage canals using quantitative susceptibility mapping,” *PloS one*, vol. 10, no. 7, p. e0132167, 2015.
- [35] Z. J. S. S. B. M. C. C. E. J. Nissi MJ, Toth F, “Susceptibility weighted imaging of cartilage canals in porcine epiphyseal growth cartilage ex vivo and in vivo,” *Magn Reson Med*, 2014.